



HAL
open science

Evidence of residual micellar structures in a lipid nanocapsule dispersion. A multi-technique approach

Emilie Roger, Florence Franconi, Tran Anh Thu Do, Carl Simonsson, Benjamin Siegler, Rodolphe Perrot, Patrick Saulnier, Jean-Christophe Gimel

► To cite this version:

Emilie Roger, Florence Franconi, Tran Anh Thu Do, Carl Simonsson, Benjamin Siegler, et al.. Evidence of residual micellar structures in a lipid nanocapsule dispersion. A multi-technique approach. *Journal of Controlled Release*, 2023, 364, pp.700-717. 10.1016/j.jconrel.2023.10.054 . hal-04295223

HAL Id: hal-04295223

<https://univ-angers.hal.science/hal-04295223>

Submitted on 20 Nov 2023

HAL is a multi-disciplinary open access archive for the deposit and dissemination of scientific research documents, whether they are published or not. The documents may come from teaching and research institutions in France or abroad, or from public or private research centers.

L'archive ouverte pluridisciplinaire **HAL**, est destinée au dépôt et à la diffusion de documents scientifiques de niveau recherche, publiés ou non, émanant des établissements d'enseignement et de recherche français ou étrangers, des laboratoires publics ou privés.

Evidence of residual micellar structures in a lipid nanocapsule dispersion. A multi-technique approach.

Emilie ROGER^(a), Florence FRANCONI^{(a)(b)}, Tran Anh Thu DO^(a), Carl SIMONSSON^(a), Benjamin SIEGLER^(c), Rodolphe PERROT^(d), Patrick SAULNIER^(a), Jean-Christophe GIMEL^{(a)(*)}

(a) **Univ Angers**, INSERM, CNRS, **MINT**, SFR ICAT, F-49000 Angers, France

(b) **Univ Angers**, **PRISM**, SFR ICAT, Biogenouest, F-49000 Angers, France

(c) **Univ Angers**, **ASTRAL**, SFR MATRIX, F-49000 Angers, France

(d) **Univ Angers**, **SCIAM**, SFR ICAT, F-49000 Angers, France

(*) Corresponding author: jean-christophe.gimel@univ-angers.fr, Tel: +33 2 4468 8529, Fax +33 2 4468 8546. Lab MINT, IBS-CHU, 4 rue Larrey, F-49933, Angers cedex, France.

Abstract

Nanoemulsions are metastable emulsions in the nanometric range which can be obtained using low-energy processes. A decade ago, it was demonstrated that a non-negligible amount of residual surfactant micelles may coexist with the oil nanodroplets in a model oil/surfactant system. Those micelles were called “wasted” micelles as they did not participate in the formation of the nanodroplets. Little attention has been focused on the potential presence or effect of such secondary structures in nanoemulsions used as drug delivery systems. Here, we present an extensive characterization of lipid nanocapsules, a nanoemulsion obtained from a medium-chain triglyceride mixed with a pegylated surfactant by a process comprising a temperature-dependent phase inversion followed by a cold-water quench. Lipid nanocapsules demonstrate a very good shelf stability. First, for clarity and academic purposes, we briefly present the pros and the cons of the various diffusion-based characterization techniques used i.e., multi-angle and single-angle dynamic light scattering, nanoparticle tracking analysis, fluorescence recovery after photobleaching, and diffusometry nuclear magnetic resonance. Then, combining all these techniques, we show that up to 40 wt% of the surfactant is not involved in the lipid nanocapsule construction but forms residual micellar structures. Those micelles also contain a small quantity of medium-chain triglyceride (2 wt% of the initial amount) and encapsulate around 40 wt% of a fluorescent dye originally dispersed in the oily phase.

Keywords

Nanomedicines, Micelles, Brownian diffusion, Nanoparticle tracking analysis (NTA), Fluorescence recovery after photobleaching (FRAP), Nuclear magnetic resonance (NMR)

List of symbols

General

| | |
|--------|---|
| D | Translational diffusion coefficient of a nanoparticle in dilute conditions in a simple liquid |
| D_c | Collective translational diffusion coefficient of a nanoparticle (using the diffusion equation) |
| D_s | Self-diffusion translational coefficient of a nanoparticle (using the random walk approach) |
| η | Viscosity of the solvent |
| k_B | Boltzmann constant |
| MSD | Mean square displacement of a Brownian nanoparticle |
| n | Refractive index |
| R | Hydrodynamic radius of a nanoparticle |
| t | Time |
| T | Absolute temperature of the solvent |

DLS

| | |
|-----------------------|---|
| $\langle D \rangle_z$ | z-average translational diffusion coefficient extracted from $G(\Gamma)$ |
| Δt | Delay time of correlation functions |
| $g_1(q, \Delta t)$ | Electric field-time correlation function of the scattered light at diffusion vector q and delay time Δt |
| $g_2(q, \Delta t)$ | Intensity-time correlation function of the scattered light at diffusion vector q and delay time Δt |

| | |
|------------------------------|--|
| $G(\Gamma)$ | Distribution function of relaxation rates Γ of the electric field-time correlation function |
| Γ | Relaxation rate |
| $\langle \Gamma \rangle$ | Average relaxation rate of $G(\Gamma)$ |
| λ_0 | Wavelength of the incident vertically polarized laser beam |
| v_G | Variance of $G(\Gamma)$ |
| PDI_G | Polydispersity index of $G(\Gamma)$ |
| q | Amplitude of the scattering vector |
| θ | Scattering angle |
| $\langle 1/R \rangle_z^{-1}$ | Average hydrodynamic radius extracted from $G(\Gamma)$ |

NTA

| | |
|---------------------|--|
| $f(R)$ | Number-size distribution function of nanoparticles with hydrodynamic radii R |
| v_f | Variance of $f(R)$ |
| PDI_f | Polydispersity index of $f(R)$ |
| $\langle R \rangle$ | Number-average hydrodynamic radius |

NMR

| | |
|---------------------|--|
| b | Diffusion weighting factor in NMR diffusometry experiments |
| δ | Magnetic gradient duration |
| Δ | Separation time between the two gradient lobes. Δ is also called the diffusion time in NMR diffusometry experiments |
| $f_{\text{NMR}}(D)$ | Distribution of diffusion coefficients D obtained by NMR diffusometry |
| G_D | Magnetic gradient amplitude |
| γ | proton gyromagnetic ratio |

| | |
|---|--|
| S_0 | NMR diffusometry signal at $b = 0$ for a given proton |
| $S(b)$ | NMR diffusometry signal at a given diffusion weighting factor b for a given proton |
| S_{Cap} | Normalized qNRM signal of Cap molecules |
| | |
| <u>FRAP</u> | |
| f | Fraction of the fluorescence recovery ratio due to micellar structures |
| I_0 | Average fluorescence intensity in the sample before bleaching |
| $I(\mathbf{r}, t)$ | Fluorescence intensity at a distance r from the center of the ROI and time t |
| $\langle I(r, 0) \rangle$ | Average initial fluorescence intensity profile |
| $I_{\text{ROI}}(t)$ | Average fluorescence intensity in the region of interest at time t |
| \mathbf{r} | Vector position in the region of interest |
| r | Distance to the ROI center |
| $\langle r_{\text{ROI}}(t) \rangle$ | Average recovery ratio in the ROI |
| $\langle r_{\text{ROI}}(t) \rangle_{\text{LNC}}$ | Average recovery ratio in the ROI due to LNC |
| $\langle r_{\text{ROI}}(t) \rangle_{\text{micelles}}$ | Average recovery ratio in the ROI due to micelles |
| ∇^2 | Laplacian operator |

List of abbreviations

| | |
|----------------------|--|
| 2D | Two-dimensional |
| 3D | Three-dimensional |
| Cap | Captex® 8000, glyceryl tricaprilate |
| CMC | Critical micellar concentration |
| DiI | 1,1'-dioctadecyl-3,3,3',3'-tetra methylindocarbocyanine perchlorate |
| DLS | Dynamic light scattering |
| DOSY | Diffusion ordered spectroscopy |
| FRAP | Fluorescence recovery after photobleaching |
| HLB | Hydrophilic-lipophilic balance |
| ILT | Inverse Laplace transform |
| Kol | Kolliphor® HS15, a mixture of free polyethylene glycol 660 and some mono and di-esters of 12-hydroxy stearic acid with polyethylene glycol 660 |
| DiI-Kol | Kol aqueous solution loaded with DiI |
| Lip | Lipoid® S75-3, a phospholipidic co-surfactant from soybean mainly made of hydrogenated phosphatidylcholine (70 wt%) |
| LNC | Lipid nanocapsule |
| DiI-LNC | LNC loaded with DiI |
| D ₂ O-LNC | LNC formulated in D ₂ O |
| NL-LNC | Non loaded LNC |
| MADLS | Multi-angle dynamic light scattering |
| MC | Monte Carlo |
| MCT | Medium chain triglyceride |
| MSD | Mean square displacement of a nanoparticle |
| NMR | Nuclear magnetic resonance |
| NP | Nanoparticle |

| | |
|---------|---|
| NTA | Nanoparticle tracking analysis |
| PDI | Polydispersity index |
| PEG | Polyethylene glycol |
| PEG-HS | Esters of 12-hydroxy stearic acid with polyethylene glycol 660 |
| PEG-HS1 | Monoester of 12-hydroxy stearic acid with polyethylene glycol 660 |
| PEG-HS2 | Diester of 12-hydroxy stearic acid with polyethylene glycol 660 |
| qNMR | Quantitative nuclear magnetic resonance |
| ROI | Region of interest |
| SADLS | Single-angle dynamic light scattering |
| THFd | Deuterated tetrahydrofuran |

1. Introduction

The nanomedicine research field mainly focuses on nanosized carriers and their potential abilities to deliver drugs or carry imaging agents within the body. However, despite a huge number of research articles on nanoparticle (NP) enabled medicinal products, only about 50 have reached the market [1,2], and very recently, mRNA COVID-19 vaccines based on lipid nanocarriers [3]. One of the main issues concerns relationships between their physicochemical properties (size distribution, surface charge, hydrophobicity, shape...) and biological events such as cellular uptake, ability to cross biological barriers, biodistribution or circulation times in the bloodstream [4]. Thus, adequate characterization of candidate nanomedicine formulations especially their particle size distribution, is of great importance. However, it is not necessarily an easy task to achieve [1,5–10].

Among those NPs, lipid nanocapsules (LNCs) have shown great promise [11]. They are formulated with pharmaceutical-grade ingredients generally recognized as safe, i.e. a medium-chain triglyceride (MCT), a pegylated surfactant, and a small amount of soy lecithin cosurfactant. They are obtained by a low-energy method based on a phase inversion temperature process combined with a rapid quench with cold water [12]. Their average hydrodynamic diameter ranges from 20 to 200 nm [13–15] and can easily be tuned by altering the surfactant-to-oil ratio. These LNCs are very stable [16] and are notably studied for pharmaceutical use. They have successfully encapsulated cytotoxic small molecules used for tumor treatment (e.g. paclitaxel, Sn38, sorafenib, decitabine, ferrocifenol...) and nucleosides for gene therapies (miRNA, SiRNA, DNA) [11,17,18]. LNCs belong to the class of nanoemulsions (metastable emulsions in the nanometric range) [19,20]. The presence of residual surfactant swollen micelles in such nanoemulsions is still an open question [21,22] and, to our knowledge, no quantitative analysis was ever made. If their presence is established in LNCs, this will raise a series of important questions regarding the use of such nanoemulsions in the drug delivery field.

In the present study, an extensive characterization of a 30 nm radius LNC dispersion was performed to gain insight into its precise nature, i.e., what kind of colloidal objects are present and how initial ingredients are distributed among these miscellaneous entities. To fulfill that objective, various techniques, widely accessible to most drug delivery research teams, were combined: multi-angle dynamic light scattering (MADLS), single-angle dynamic light scattering (SADLS), nanoparticle tracking analysis (NTA), fluorescence recovery after photobleaching (FRAP), and nuclear magnetic resonance (NMR) spectroscopy and diffusometry. Most of these techniques rely on the measurement of the NP translational diffusion coefficient. For polydisperse dispersions, they usually lead to an average value, but for some of them (DLS and NTA) to a more or less accurate determination of the diffusion coefficient distribution. Under the hypothesis of dilute

dispersions in a simple liquid, the zero-concentration translational diffusion coefficients (D) can be converted to a hydrodynamic radius (R) using the well-known Stokes-Einstein equation in which T is the absolute temperature, η the solvent viscosity, and k_B the Boltzmann constant (**Eq. (1)**).

$$R = \frac{k_B \cdot T}{6\pi \cdot \eta \cdot D} \quad (1)$$

As detailed in the following, these techniques have their own benefits and drawbacks restraining the scope of the conclusions when used individually [23]. But combined, and associated with a separation technique, like ultracentrifugation used here, they are shown to be very powerful [10].

2. Theoretical background of diffusion and characterization methods

2.1. Diffusion phenomena

Diffusion phenomena of NPs result from erratic Brownian motions due to continuous thermal collisions of NPs with solvent molecules. Two different theoretical approaches can be used to model the diffusion of NPs. Both assume independent random displacements but lead to the definition of two different diffusion coefficients [24]: (i) the self-diffusion coefficient, D_s , extracted from the knowledge of individual particle trajectories; (ii) and the collective diffusion coefficient, D_c , sometimes called mutual diffusion coefficient in the literature, obtained from the temporal evolution of the nanoparticle concentration profile. Both have the same unit (m^2/s) but relate very different physical quantities: the mean square displacement (MSD) to the time for D_s , and a particle concentration gradient dependent flux for D_c (known as Fick's law or diffusion equation). For highly diluted dispersions (below $\sim 0.5\%$ volume fraction in practice for the Brownian hard sphere model [25,26]), D_s and D_c are equal and will be referred to as D in the following. Then, in a simple liquid, a characteristic hydrodynamic size can be derived using **Eq. (1)**. But D_s and D_c have very different behavior as the concentration increases. D_s is always a monotonous decreasing function of the NP concentration while D_c can first increase and then decrease with the concentration depending on the type of interparticle interactions [25,26]. Both D_s and D_c tend to zero at very high concentrations due to steric hindrances that freeze particle motions. As will be explained below, DLS and FRAP experiments give access to D_c while NMR diffusometry and NTA measure D_s . The low concentration limit is not only mandatory to extract a size from the knowledge of D using the Stokes-Einstein relation, but it is also a strong hypothesis for some experimental techniques, especially for light scattering and particle tracking.

2.2. Dynamic light scattering (DLS)

DLS is an old characterization technique introduced in the '70s [27] and is intensively used since. It was made available to a large community of routine users by developing low-cost automated single-angle DLS instruments. But, they still require appropriate operating procedures for accurate results [28]. This part briefly explains the DLS theory and highlights the necessary precautions to be taken when using this technique. More details are given in the supplementary material (see **S1**).

With no external field (at rest), the motions of NPs dispersed in a solvent are only driven by the thermal agitation. DLS is based on analyzing the resulting intensity fluctuations of the scattered light from the dispersion when illuminated by a polarized laser beam with wavelength λ_0 . More specifically, the apparatus measures g_2 , the intensity-time correlation function of the scattering

intensity. It quantifies the average degree of correlation of the scattered light between two instants separated by a delay time Δt , at an observation angle θ between the incident beam and the scattered light. When Δt is very small compared to sample dynamics, the scattered intensity has weakly varied and g_2 is maximum. But, as Δt increases, motions of the scattering species become significant, and the average correlation between two instants vanishes rapidly. g_2 is a fast-decreasing function of Δt and is usually represented on a logarithmic scale of Δt .

The choice of θ is very important, it defines the length scale at which dynamics are probed. Formally, this length scale depends both on the particle size, R , and on the scattering vector, defined as the difference between the incident and the scattered wave vectors. Its amplitude, q , is given by $q = (4\pi \cdot n)/\lambda_0 \cdot \sin(\theta/2)$, with n the refractive index of the solvent, and q^{-1} has the dimension of a length. See **Fig. S1.1** in the supplementary material for more details. As an example, for an aqueous dispersion, using a 660 nm laser, and varying θ from 20° (front scattering) to 150° (back scattering) changes the probe length scale from around 200 nm to around 40 nm, corresponding to a $5 \times$ magnification. When $q \cdot R \ll 1$ (corresponding to θ or q small enough and called thereafter the small q limit), the sample is observed at large length scales and NPs are seen as dimensionless scatterers. The scattered intensity is maximum and the decorrelation of g_2 results only from translational Brownian motions. For large NPs or large θ , the small q limit may not be achieved, and in that case internal structures are also probed. Therefore, the g_2 decorrelation results not only from the Brownian translational motions but also from possible faster internal modes (such as internal dynamics for polymer chains or rotational Brownian motions for optically anisotropic particles like gold NPs).

From the point of view of statistical physics, the scattered intensity is a delicate quantity to handle, and the electric field-time correlation function, g_1 , is preferred. Assuming a Gaussian statistic for the amplitude of the scattered electric field, g_2 is simply related to g_1 by the so-called Siegert relation [29]: $g_2(q, \Delta t) = 1 + g_1(q, \Delta t)^2$.

For a monodisperse sample in the small q limit (with particle size smaller than q^{-1}), and if no multiple scattering nor fluorescence emission occurs, it can be shown that g_1 is a simple exponential decay of Δt [29], depending on the collective diffusion coefficient, D_c . In the low concentration limit, D_c is substituted by D , see **Eq. (2)**.

$$g_1(q \rightarrow 0, \Delta t) = \exp(-D \cdot q^2 \cdot \Delta t) \quad (2)$$

with $\Gamma = D \cdot q^2$, the relaxation rate of the exponential decay.

Normally, it is necessary to perform multi-angle measurements to evaluate Γ for various q^2 and check the expected linear dependency at small q . Then, its slope gives D , and the hydrodynamic

radius can be calculated using **Eq. (1)**. If the small q limit is not respected for optically anisotropic NPs or polymer chains, faster relaxation rates appear and the sample can be wrongly interpreted as polydisperse, especially when single-angle measurements are performed at large angles [28].

The main disadvantage of DLS is the extreme sensitivity to the biggest particles, making its use tricky for characterizing polydisperse systems or dusty samples. In the small q limit, the contribution of each NP to the scattering intensity is proportional to the square of its volume ($\propto R^6$) [30]. Thus, an NP with a ten-time bigger size weighs a million times more in the scattering at small angle. For the polydisperse case, even for rigid isotropic objects, the constraint q^{-1} bigger than the biggest particle size becomes mandatory. It allows to ignore the NP form factors that attenuate the R^6 weighting of the biggest NPs and would lead to the measurement of an undetermined average diffusion coefficient [28]. Thus, $g_1(q \rightarrow 0, \Delta t)$ becomes a sum of exponentials where each NP contributes to the decay of g_1 with its own Γ and a weighting factor proportional to R^6 . This leads to a distribution of relaxation rates: $G(\Gamma)$ and **Eq. (2)** is rewritten as **Eq. (3)**.

$$g_1(q \rightarrow 0, \Delta t) = \int_0^{\infty} G(\Gamma) \cdot \exp(-\Gamma \cdot \Delta t) \cdot d\Gamma \quad (3)$$

Using the cumulant analysis method [31,32], one can easily extract from $g_1(q, \Delta t)$ the average relaxation rate $\langle \Gamma \rangle$ and the variance v_G of the distribution $G(\Gamma)$. Then, the z-average diffusion coefficient, $\langle D \rangle_z$, is obtained from the slope of the evolution of $\langle \Gamma \rangle$ as a function of q^2 in the limit $q \rightarrow 0$ (see **Eq. (4)**).

$$\langle \Gamma \rangle = \langle D \rangle_z \cdot q^2 \quad (q \rightarrow 0) \quad (4)$$

Using **Eq. 1**, the inverse of the z-average inverse hydrodynamic radius, $\langle 1/R \rangle_z^{-1}$, is formally obtained (see **Eq. (5)**). It is abusively called z-average hydrodynamic radius for simplicity.

$$\langle 1/R \rangle_z^{-1} = \frac{k_B \cdot T}{6\pi \cdot \eta \cdot \langle D \rangle_z} \quad (5)$$

From the determination of the variance of $G(\Gamma)$, a dimensionless quantity characterizing the polydispersity is calculated as the ratio of the variance by the square of the mean. It is called the polydispersity index (PDI), see **Eq. (6)**. The subscript G means it is related to the function $G(\Gamma)$.

$$PDI_G = \frac{v_G}{\langle \Gamma \rangle^2} \quad (6)$$

Another approach would consist in extracting directly $G(\Gamma)$ by performing an inverse Laplace transform (ILT) of $g_1(q, \Delta t)$. But, performing an ILT is a very delicate and ill-conditioned mathematical routine, highly sensitive to the noise in the data [33]. Even if many algorithms have

been developed like REPES [34], CONTIN [35], SBL [36], or the recent CORENN [37,38], using an ILT algorithm to extract a distribution function from DLS data is usually not recommended without prior knowledge about the shape of the distribution (mono or multimodal distribution).

To conclude, DLS measurements should be realized at sufficiently low NP concentrations (no multiple scattering nor steric hindrances for particle motions) with no laser-triggered fluorescence emission. Multi-angle measurements are necessary to assess the q^2 linearity domain of the measured values of $\langle \Gamma \rangle$ (see **Eq. (4)**). This allows a confident calculation of the z-average diffusion coefficient and its corresponding average hydrodynamic radius. The small q limit is mandatory except for monodisperse, rigid, and optically isotropic NPs. Otherwise, at larger q (larger θ or smaller length scales), internal NP dynamics are probed for non-rigid or optically anisotropy particles, and, for NPs with sizes bigger than q^{-1} , the R^6 weighting factor is not achieved. This leads to an overestimation of the z-average diffusion coefficient (underestimation of the average hydrodynamic radius) combined with a wrong determination of the polydispersity index (either over or underestimated). In practice, when using SADLS with a backscattering detector ($\theta = 173^\circ$) to probe rigid and optically isotropic polydisperse NP sample, a correct determination is obtained when particles have radii no bigger than about 50 nm and PDI_G not bigger than 0.1.

2.3. Nanoparticle tracking analysis (NTA)

In contrast to DLS which analyzes the total light scattered by the NP population, NTA is focused on individual particles. NTA is a recent optical microscopy technique [39,40] that monitors particle trajectories using an optical microscope. A small volume of a very dilute NP dispersion (around 10^8 - 10^9 NPs/mL equivalent to around $5 \cdot 10^{-5}$ - $5 \cdot 10^{-4}$ % volume fraction for 100 nm diameter particles) is illuminated with a laser beam. NPs scatter the laser light, and depending on their size, refractive index, and position in the focal plane appear as more or less bright spots in the microscope field of view. Movies are recorded with a CCD camera and processed to build individual two-dimensional (2D) trajectories, projections on the focal plane of their 3D motion. To identify unambiguously individual trajectories only 10 to 100 particles must be present in the microscope field of view. Measurements are performed under flow with a syringe pump to increase the sampling rate. The Brownian component of each trajectory is extracted, and the corresponding self-diffusion coefficient is obtained for each detected particle using the relation between its MSD and the time $MSD = 4 \cdot D_s \cdot t$. As the concentration of NP is very low, this technique gives direct access to D and thus to the corresponding hydrodynamic radius R of each detected NP.

The detection of an NP results from the amount of light it scatters. Then, the corresponding spot brightness depends on (i) the NP square volume, (ii) the square difference of refractive index with the solvent, (iii) and the position of the NP from the focal plane. Depending on the detector sensitivity and the threshold used to qualify a detected particle, small particles or particles with low optical contrast can elude the detection. This technique gives direct access to a number distribution $f(R)$ of detected NPs. Then, various average quantities are calculated like the number-average hydrodynamic radius $\langle R \rangle$ and the variance v_f of the distribution. A polydispersity index can also be defined: $PDI_f = v_f / \langle R \rangle^2$.

Moreover, as the exact illuminated sample volume is known, the number concentration of the detected particles can be calculated for each histogram bin. Assuming spheres with densities close to unity, a mass-balance can easily be computed and compared to the total amount of ingredients used to formulate the dispersions.

2.4. NMR diffusometry

NMR diffusometry is a 2D NMR technique to estimate self-diffusion coefficients related to each proton resonance, also often named pulse-field gradient NMR or diffusion-ordered spectroscopy (DOSY). It is based on the work of Stejskal and Tanner in the mid-60s [41]. As both physical and chemical information are obtained in a single experiment, NMR diffusometry can be used as a virtual separation method on a nanoparticle mixture with various hydrodynamic sizes. The ^1H nuclei signal decay, induced by self-diffusion between two lobes of magnetic field gradients, is measured as a function of the diffusion weighting factor b . Considering the NMR sequence used [42], b is given by $b = \gamma^2 \cdot \delta^2 \cdot G_D^2 \cdot (\Delta - \delta/3)$, with γ the proton gyromagnetic ratio, G_D the diffusion sensitizing magnetic gradient amplitude, δ the magnetic gradient duration, and Δ the separation time between the two gradient lobes. Δ is also called diffusion time as it represents the time scale over which the diffusion is probed. For a given NMR peak (corresponding to a given proton signal), the signal decay, $S(b)$, is described as a sum of exponential decays, with S_0 being the signal amplitude in the absence of diffusion sensitizing gradients (see **Eq. (7)**) [41].

$$S(b) = S_0 \cdot \int_0^\infty f_{\text{NMR}}(D_s) \cdot \exp(-D_s \cdot b) \cdot dD_s \quad (7)$$

D_s is the self-diffusion coefficient of each proton nano carrier weighted by a distribution function, $f_{\text{NMR}}(D_s)$, which depends on the amount of the given proton in each NP but also on the spin relaxation of these protons in a given carrier [43]. The latter tends to lower the contribution of slow diffusing carriers, making distribution function quantification delicate and accessible only

with advanced acquisition strategies [44]. Moreover, as the NMR signal is proportional to the volume concentration, accurate estimates require enough concentration possibly leading to “hindered” self-diffusion coefficient estimation ($D_s < D$). This can be solved by performing NMR diffusometry experiments with various sample concentrations to determine D by extrapolating D_s at zero concentration. Besides a good signal-to-noise ratio, a good estimate accuracy on the diffusion coefficient distribution also requires sampling over the correct b range [45]. b has the dimension of the inverse of a diffusion coefficient (s/m^2) and is analogous of $q^2 \cdot \Delta t$ in DLS. In NMR diffusometry experiments the accessible square gradient amplitude range is only about 3 decades while in MADLS experiments, the delay time window runs over nearly 10 decades, and the use of different angles allows to easily shift the relaxation of $g_1(q, \Delta t)$ in this temporal window. Again, ILT routines can be used to extract $f_{\text{NMR}}(D_s)$ from the signal decay of a given proton with increasing b . When dealing with NP mixtures, the determination of each diffusion coefficient component contribution to one signal decay can be tricky [45]. Fortunately, accuracy can be improved by using a multivariate approach that takes advantage of the covariance between the resonances of the different protons carried by the same NP [46,47]. Decays of all resonance peaks are simultaneously fitted with a discrete sum of exponential decays. The number of components (diffusion coefficients) is fixed *a priori* and some knowledge about the expected number of diffusing species is required. Here, the SCORE routine has been used [48]. It gives access not only to the calculation of the various D_s but also to the contribution of each component to the total spectrum. This second information is very important to identify the chemical nature of each diffusing specie.

2.5. Fluorescence recovery after photobleaching (FRAP)

FRAP is a confocal laser scanning microscopy technique that gives insight into the dynamical behavior of fluorescent dyes at the microscopic level. It was first developed in the mid-70s on widefield fluorescence microscopes [49,50] and transposed in the ‘90s to confocal laser scanning microscopes [51]. It has been successfully applied to various systems, including living cells, to measure 2d or 3d diffusion coefficients, interaction/binding constants, etc. [52]. In a FRAP experiment, a sample consisting of fluorescently labeled molecules or particles is placed in a sealed compartment and imaged using a confocal microscope with its laser light source set at a relatively low output intensity. Then the fluorescence is irreversibly suppressed in a region of interest (ROI) of the sample by illuminating the ROI with the laser set at its maximum output intensity. By monitoring the recovery of the fluorescence in the ROI, i.e. the diffusion of non-bleached molecules or particles into the bleached ROI, various parameters related to the mobility of the labeled molecules or particles can be extracted. Considering a monodisperse dispersion of

fluorescent NPs at thermal equilibrium in a simple liquid, several assumptions must be fulfilled to extract the diffusion coefficient and to calculate the hydrodynamic radius of the NPs from the fluorescence recovery data. (i) The fluorescence intensity of a pixel should be proportional to the NP concentration in that pixel. This is generally achieved for dilute NP dispersions using a low laser intensity providing a fluorescent signal within the linear range of the detector. In this way, variations in the fluorescence intensity are directly proportional to variations in the concentration of fluorescent NPs. (ii) No advective motion driven by evaporation or thermal gradient should be observed, thus the sample must be perfectly sealed in a temperature-controlled environment. (iii) The NPs should only undergo uncorrelated Brownian motions. They should not interact with each other nor with surfaces where adsorption could take place. This is achieved by using low-concentration NP dispersions and by choosing an ROI far from any edges. Under these assumptions, the average fluorescence recovery is only governed by the diffusion equation (**Eq. (8)**) where D is used instead of D_c as the concentration is very low.

$$\frac{\partial}{\partial t} I(\mathbf{r}, t) = D \cdot \nabla^2 I(\mathbf{r}, t) \quad (8)$$

Here $I(\mathbf{r}, t)$ is the fluorescence intensity at position \mathbf{r} in space at time t , and ∇^2 is the Laplacian operator. In theory, predicting the temporal evolution of the fluorescence intensity in the ROI, $I_{\text{ROI}}(t)$, only requires some knowledge about the initial conditions $I(\mathbf{r}, 0)$ right after the bleach. Unfortunately, the diffusion equation is difficult to handle and can only be solved explicitly for a limited number of initial conditions, and in lower dimensional spaces [53]. Phenomena that take place under the microscope slide must be reduced to a 2d or even a 1d problem. This implies additional assumptions to be experimentally fulfilled. For example, the use of a low numerical aperture objective with a circular ROI leads to bleached profiles with cylindrical symmetry [52]. Combined with the hypothesis of isotropic diffusion, the problem turns into a 1d representation. Thus, only the radial profile, $I(r, t)$, with respect to the distance r from the center of the ROI is to be considered. But to be solvable, the initial imprint must also comply with a Gaussian-like shape [54]. This is not always the case, especially with fragile dyes for which an inversed top-hat profile is usually obtained right after the bleach. Thus, to apply a fitting model either on the average intensity in the ROI, $I_{\text{ROI}}(t)$, like proposed by Kang et al. [54], or on the complete radial profile like Jonasson et al. [55], the first recovery images have to be discarded until a Gaussian-like profile is recovered. Unfortunately, these images are the most interesting in terms of fluorescence recovery ratio, and omitting them could lead to a less accurate determination of D . Jonasson et al. [56] have proposed an extension of their pixel-based method but it is limited to monotonic increasing radial profiles. In the present paper, these issues are circumvented by using a homemade Monte Carlo (MC) simulation. It is based on the same assumption used to derive Fick's laws: that is NPs undergo only uncorrelated random motions. It allows to calculate D in an easy way whatever the

initial bleaching conditions. A very similar approach was proposed by Blumenthal et al. [57] to calculate the 2d diffusion coefficient of dye in cellular membranes. The MC simulation details are described in supporting information (see **S2**).

Starting from an initial condition where the ROI is imprinted by a full power laser beam, a FRAP experiment consists of monitoring, pixel by pixel, the fluorescence recovery of the image as a function of the time t . The system being isotropic and having cylindrical symmetry, such an experiment gives access to the temporal evolution of intensity radial profile $I(r, t)$ with $I(r, t < 0) = I(r \rightarrow \infty, t) = I_0$, where I_0 is the reference fluorescence intensity before the bleach, proportional to the macroscopic number concentration of NP in the sample. Here, $t < 0$ and $r \rightarrow \infty$ correspond to moments before the bleach, and regions far from the ROI, respectively. Then, FRAP data consists in a sequence of pixelized grayscale images. The 1st image ($t < 0$) represents the system just before the bleach and is used to define I_0 . It is also used in post-treatment to correct the rest of the series for uneven illumination [58] and photofading issues [52]. The 2nd image is scanned just after the bleach and corresponds to $t = 0$. Then, other images are scanned at regular time intervals until the average intensity in the ROI, $I_{\text{ROI}}(t)$, recovers a value close to I_0 . After the post-treatment, $I(r, t)$ and $I_{\text{ROI}}(t)$ are computed for each image and are expressed on a normalized intensity scale ranging from 0 to 1 where unity is used for I_0 . To reduce the intrinsic high noise level present in confocal data, several independent FRAP experiments are performed at different locations chosen randomly in the sample and far from any edges. Then, an average initial profile $\langle I(r, 0) \rangle$ and an average recovery ratio $\langle r_{\text{ROI}}(t) \rangle$ can be computed with $r_{\text{ROI}}(t) = (I_{\text{ROI}}(t) - I_{\text{ROI}}(0)) / (I_0 - I_{\text{ROI}}(0))$. The obtained recovery data are then fitted either with the Kang et al. model [54] or using the homemade MC algorithm (**S2**).

Unfortunately, FRAP experiments cannot manage polydispersity issues, mainly for two reasons: the intrinsic high noise level in the data and the lack of a clear relationship between the hydrodynamic size of a NP and its contribution to the total fluorescence. Thus, only an “average” diffusion coefficient can be determined. It is weighted by the fluorescence level of each kind of fluorescent NP diffusing in the system.

3. Experimental section

3.1. Chemicals

Captex® 8000 (glyceryl tricaprilate), an MCT, was kindly provided by Abitec Corp. (Columbus, OH, USA). Kolliphor® HS15, a pegylated surfactant (a mixture of free polyethylene glycol 660 and some mono and di-esters of 12-hydroxy stearic acid with polyethylene glycol 660) was purchased from BASF (Ludwigshafen, Germany). The certificate of analysis gives 32.7 wt% of free polyethylene glycol (PEG) for the batch used here (n° 32384609T0). No information was given about mono and di-esters composition. This is a hydrophilic surfactant with an hydrophilic-lipophilic balance (HLB) around 15 and a critical micellar concentration (CMC) in water between 50 and 200 µg/mL [59]. Lipoid® S75-3 is a phospholipidic co-surfactant mainly made of 70 wt% hydrogenated phosphatidylcholine from soybean. It was purchased from Lipoid GmbH (Ludwigshafen, Germany). This is a lipophilic surfactant with an HLB below 10 [60]. Maleic acid, NaCl, D₂O 99.9 % D, and deuterated tetrahydrofuran-d₈ ≥ 99.5 % D (THFd) were purchased from Merck (Darmstadt, Germany). The fluorescent dye DiI (1,1'-dioctadecyl-3,3,3',3'-tetramethylindocarbocyanine perchlorate, ref. D282) and 30 nm radius polystyrene nanosphere size standards (ref. 3060A) were purchased from Thermo Fisher Scientific (Waltham, MA, USA). Ultrapure water was obtained from a Milli-Q® Advantage A10 System (Merck Millipore, Darmstadt, Germany).

In the following, Cap, Kol, Lip, PEG-HS1, and PEG-HS2 will be used for Captex® 8000, Kolliphor® HS15, Lipoid® S75-3, mono and di-ester hydroxy stearate of PEG, respectively. PEG-HS will be used to designate indifferently PEG-HS1 or PEG-HS2.

3.2. Sample preparation

3.2.1. LNC formulations

Non-loaded LNC (NL-LNC) dispersions were prepared according to the phase inversion method thoroughly described elsewhere [14,61]. Briefly, the lipid phase was first prepared by mixing 1600 mg of Cap with 90 mg of Lip at 70°C. Then, the aqueous phase, i.e. water 2400 mg, Kol 1333 mg (corresponding to 463 mg of free PEG and 897 mg of PEG-HS), and NaCl 98 mg was mixed with the lipid phase. NaCl (corresponding to around 0.7 M) was added to decrease the lower critical solubility temperature of the surfactant PEG block, resulting in a lowering of the phase inversion temperature to around 78°C. The mixture underwent three cycles of heating and cooling between 90°C and 70°C. During the final cooling phase, at 78 °C, 2670 mg of cold water (4°C) was added to quench the system. Fluorescent DiI-LNC formulations were obtained by

dissolving DiI in Cap (1 mg per gram of Cap) prior to the preparation of the LNCs as described above. D₂O-LNC formulations for NMR diffusometry experiments were obtained by substituting H₂O by the same volume of D₂O, taking into account its higher density (1.1 g/mL at 20°C [62]). All LNC formulations were filtered using 0.22 µm Millex® syringe filters (Merck Millipore, USA).

3.2.2. Kolliphor solutions

Various solutions of Kol, in H₂O, in D₂O (D₂O-Kol) or loaded with DiI (DiI-Kol, 1 mg DiI per gram of Kol) were prepared for comparison purposes.

3.2.3. Separation of the micellar fraction from LNC

1.8 mL of LNC or Kol formulations were added to 2.2 mL polypropylene centrifuge tubes (ref. 347357, Beckman Coulter, Villepinte, France) and ultracentrifuged at 259 000g for at least 8h using an Optima™ MAX XD Ultracentrifuge (BeckmanCoulter Inc., Brea, CA, USA) with a TLS-55 rotor. As Cap has a density close to 0.95 g/mL, LNCs creamed, and were concentrated in the supernatant, opening the door to the identification of other species present in the undernatant. To avoid any subsequent redispersion of the supernatant into the undernatant, no break was used during the deceleration step at the end of the centrifugation, and tubes were carefully deep-frozen in liquid nitrogen right after. The lower 40 vol% of the sample was separated from the upper volume by cutting the frozen tube in half. Then undernatants were thawed at room temperature and prepared for further analysis.

3.2.4. Freeze-drying of the undernatant and qNMR analysis in THFd

The recovered undernatants from the ultracentrifugation step were freeze-dried. Then the lyophilizates were weighted and redispersed in 1.5 mL of THFd followed by a short centrifugation to remove precipitated NaCl (non-soluble in THF). 0.5 mL of the supernatant was collected and mixed with 0.4 mL of THFd and 0.1 mL of a 100 mM maleic acid THFd solution, leading to a final concentration of 10 mM maleic acid and a 2-fold dilution of the original 1.5 mL redispersed undernatant. Maleic acid was used as an internal standard to perform quantitative NMR (qNMR). A calibration curve was established with 5 solutions of Cap in THFd (10 mM maleic acid) with concentrations 1.25, 2.5, 3.75, 5, and 6.25 mg/mL. Due to the complex composition of Kol, (presence of free PEG and unknown molecular composition for mono and di-esters), no quantitative analysis was performed on that compound and only the ratio mono/di-esters was calculated for Kol solutions and compared to the undernatants.

3.3. Experimental setups

3.3.1. DLS

MADLS was performed on some relevant LNC samples to check their angular dependency. An LS Spectrometer equipped with a High-Performance DPSS 500 mW, 660 nm Cobolt laser and a goniometer (LS Instruments AG, Fribourg, Switzerland) was used. Samples were prepared under a laminar flow hood and dust free 10 mm glass cylindrical cells were used. Measurements were performed at 20°C using 20 angles ranging from 20° to 150°, equally spaced on a q^2 scale with 3 measurements of 180 s at each angle.

SADLS measurements ($\theta = 173^\circ$) were systematically performed on all formulated samples using a Malvern Zetasizer® apparatus (Nano Series ZS, Malvern Panalytical, Worcestershire, UK) equipped with a 4 mW 633 nm laser. Measurements were carried out at 25°C using automatic setup and disposable cuvettes.

All samples were sufficiently diluted with pure water (filtered on 20 nm Anotop® filters) to suppress steric hindrances and multiple scattering, and then filtered on 200 nm Anotop® filters to reduce the contamination from dust particles. For LNC samples, a 1/4 000th dilution was used, corresponding to around 40 µg/mL of Kol. Pure Kol samples were prepared at 0.4 wt% and filtered on 100 nm Anotop® filters. Three measurements were performed on each sample and the cumulant method was used to analyze the results (see 2.2). Viscosity values used for water were 1.002 mPa·s at 20°C and 0.890 mPa·s at 25°C [63]. The excitation wavelength of DiI being close to 549 nm, no fluorescence emission was triggered with laser wavelengths of 633 nm nor 660 nm during DLS experiments.

3.3.2. NTA

NTA measurements were performed with a NanoSight NS300 (Malvern Panalytical, Worcestershire, UK), equipped with a 20 × objective, a 405 nm laser, and a syringe pump. Data were captured and analyzed using the software NTA 3.2 Dev Build 3.2.16. The microscope field used for detection was 100 µm × 80 µm. Samples were highly diluted (1/2 000 000th) with pure water filtered with 100 nm Anotop® filters to reduce the contamination from dust particles. They were injected in the measurement cell using a 1 mL syringe at a 100 µL/min flow rate. Five movies of 60 s each were recorded for each sample and an average number-size distribution was built from thousands of valid particle trajectories (around 5 000 per movie). The software returns histograms with an equal bin width of 0.5 nm for the hydrodynamic radii. Then, the number-average hydrodynamic radius and the variance of the distribution were computed (see 2.3). Experiments were performed at room temperature. The cell temperature was automatically recorded during the runs and the corresponding water viscosity values were given by the

software. It must be noted that the sensitivity of the CCD camera was set to its maximum value (camera level 16) but still, some LNCs appeared very dim and probably eluded the detection. In practice, LNCs with radius smaller than 20 nm are hardly detected. The detection threshold was set to the smallest acceptable level (level 5) below which spurious particle detections occur due to the CCD camera noise level.

3.3.3. ^1H NMR spectroscopy

^1H NMR spectra were acquired on a 500MHz Avance III HD NMR spectrometer (Bruker, France) equipped with a 5 mm-Broadband Observe probe. The assignment of the ^1H NMR signals to Cap and Kol was performed according to chemical shifts in agreement with the literature (see for example [64] part 6.5) and confirmed by 2d NMR analysis (see part **S3** in supplementary material for details).

For diffusometry, the maximum gradient intensity was $0.535 \text{ T}\cdot\text{m}^{-1}$. Experiments were recorded with the stimulated echo sequence with longitudinal Eddy current delay pulse sequence [42], *ledgp2s*, with at least 8 averages for each spectrum and a diffusion time Δ of 200 ms. The gradient magnitude ranged from 5 to 95 % of the maximum gradient intensity with various gradient duration $\delta = 4, 6$ or 8 ms and 128 linear gradient sampling points. Samples were prepared in D_2O at dry matter concentrations ranging from 1 to 39 wt%. All experiments were performed at 25°C . A viscosity value of $1.096 \text{ mPa}\cdot\text{s}$ for D_2O at 25°C was taken [62]. The SCORE routine was used to analyze results (see **2.4**)

qNMR data were acquired using basic one-dimensional pulse sequence with 15 ppm spectral width, 64 scans, 10 s relaxation delay, 4.37 s acquisition time, 65536 complex points, and a pulse angle of 30° . Maleic acid was used as an internal standard.

3.3.4. FRAP

FRAP experiments were performed on a Leica TCS SP8 AOBS confocal laser scanning microscope (Leica, Wetzlar, Germany) using the module of LAS X software. All acquisitions were performed using a HC PL Fluotar 10x objective with a small numerical aperture ($\text{NA}=0.3$) and the Leica FRAP booster. 512×512 pixels images were acquired at 400Hz with a 3.5 x zoom factor and the pinhole set to one Airy unit, giving a $0.650 \mu\text{m}$ pixel size and a pixel dwell time of $1.2 \mu\text{s}$. Samples were diluted in ultrapure water (0.4 wt%) and $65 \mu\text{L}$ were sealed using $1.5 \times 1.6 \text{ cm}$ Gene frame[®] systems (Thermo Fisher Scientific, USA) between regular cover glasses and glass slides. The microscope was placed in a thermostatic chamber at a temperature close to 30°C . A water viscosity value of $0.797 \text{ mPa}\cdot\text{s}$ at 30°C was used [63]. For each FRAP experiment, 3 pre-bleach images were recorded using the 488 nm laser line (40 mW) from an Argon ion laser. Then, the bleaching was achieved in a single step with the AOBS set at 100 % transmission for five lines

from the Argon ion laser: 458 nm (5 mW), 476 nm (4 mW), 488 nm (40 mW), 496 nm (6 mW) and 514 nm (10 mW). To increase the bleaching efficiency, the Leica “Zoom-In” function was used. It minimizes the scan field and concentrates the laser output light to the bleach region. The bleached ROI consisted of a 60 μm diameter disc placed in the center of the image. To reduce the intrinsic high noise level present in confocal data, n=6 independent FRAP experiments were performed at different locations chosen randomly in the sample, and far from any edges.

3.3.5. Fluorescence measurements

The fluorescence of DiI-Kol, DiI-LNC native dispersions, and ultra-centrifugated fractions were recorded at room temperature using a FluoroMax®-4 spectrophotometer (HORIBA Jobin Yvon Inc., New Jersey, USA). For DiI, the excitation wavelength was set to 548 nm, with a 3 nm excitation slit. Emission spectra were collected from 555 nm to 650 nm with a 1 nm wavelength increment, an integration time of 0.5 s, and a 2 nm slit. The fluorescence intensity was collected at the maximum peak emission (568 nm for DiI). All measurements were corrected for the lamp source fluctuations and the wavelength-dependent response of the emission monochromator. All samples were diluted, if necessary, to reduce their absorbance at 548 nm below 0.13 to be in the linear regime of both the fluorescence response and the photomultiplier.

3.3.6. Statistical errors

Statistical errors are expressed as 95 % confidence intervals, otherwise their meaning is specified in the text.

4. Results and discussion

4.1. Identification of the species in the formulation

The main objective of this study was to identify the possible existence of residual PEG-HS micellar structures in an LNC formulation, often proposed as a potential drug delivery system.

4.1.1. DLS

Fig. 1 shows results from a MADLS experiment on a typical very dilute ($1/4\ 000^{\text{th}}$) aqueous NL-LNC dispersion at 20°C . $\langle\Gamma\rangle$ was obtained at each angle using the cumulant method. A linear dependence on q^2 is observed demonstrating the presence of Brownian scatterers in the dispersion. Using **Eqs. (4), (5), and (6)**, a fit to the data gives $\langle 1/R \rangle_z^{-1} = 30.3 \pm 0.1$ nm. Averages over values obtained for the last ten angles (from 91° to 150°) give a $\text{PDI}_g = 0.035 \pm 0.007$. No deviation from the q^2 -law was observed on the whole q -range and thus, measured hydrodynamic radii have no angular dependency. Star symbols in **Fig. 1** show three measurements of $\langle\Gamma\rangle$ performed on the same sample at 173° using SADLS (corrected for temperature and laser wavelength differences). Their average value is located 2% above the red dashed line and is in very good agreement with MADLS measurements. Thus, the mandatory low q limit is fulfilled for NL-LNC dispersions, and in the following, fast SADLS measurements were used confidently to characterize all samples formulated in this study.

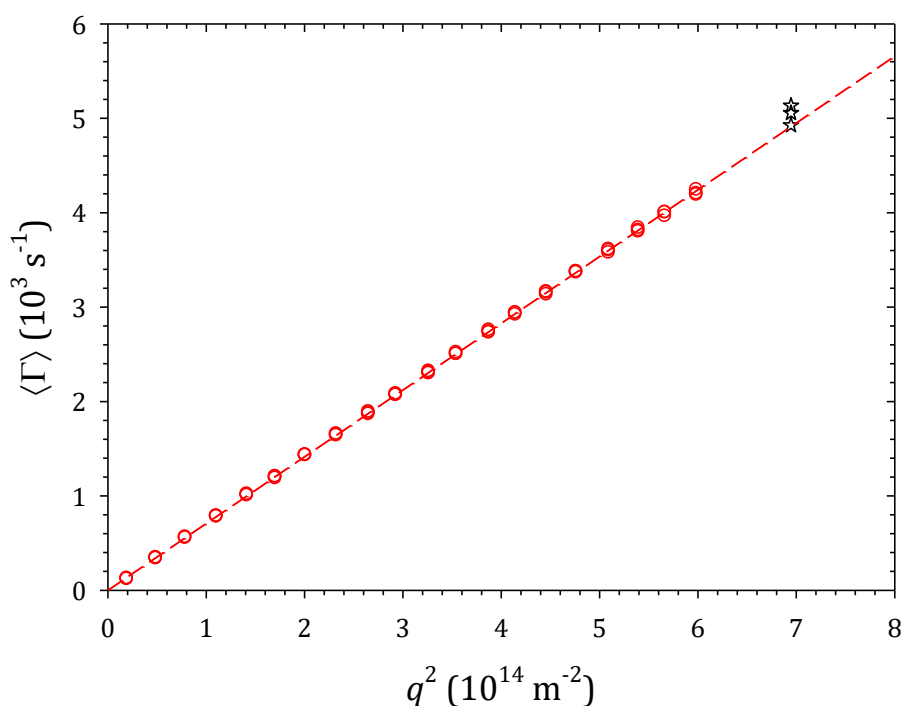


Figure 1. DLS: Evolution of $\langle\Gamma\rangle$ (red open circles) as a function of q^2 for a $1/4\ 000^{\text{th}}$ diluted dispersion of NL-LNC in water at 20°C . Stars represent values of $\langle\Gamma\rangle$ obtained at $\theta = 173^{\circ}$ with SADLS. All measurements were performed in triplicates for each angle. The red dashed line is a linear fit to MADSL data (red open circles).

No significant size nor polydispersity difference were observed between NL-LNC formulated in water, DiI-LNC, or D₂O-LNC. The results are presented in **Table 1**. As a comparison, the size of PEG-HS micelles (Kol solution) is also given.

Table 1

DLS: Comparison of $\langle 1/R \rangle_z^{-1}$ and PDI_G obtained by the cumulant method using SADLS for various formulations.

| | $\langle 1/R \rangle_z^{-1}$ (nm) | PDI_G |
|----------------------------|-----------------------------------|-------------------|
| NL-LNC (n=5) | 29.1 ± 0.6 | 0.060 ± 0.022 |
| DiI-LNC (n=7) | 29.1 ± 0.7 | 0.074 ± 0.015 |
| D ₂ O-LNC (n=3) | 29.7 ± 3.2 | 0.084 ± 0.065 |
| Kol micelles (n=3) | 6.0 ± 0.2 | 0.032 ± 0.042 |

The DLS average size of LNC samples remained stable with dilution and no significant difference was observed between dilutions above the Kol CMC (1/400th, equivalent to around 400 µg/mL of Kol), or below (1/4 000th, around 40 µg/mL of Kol).

4.1.2. NTA

The number-size distribution, $f(R)$, obtained by NTA on the same NL-LNC formulation analyzed by MADLS is plotted in **Fig. 2**. It is averaged over five measurements on the same sample. It gives $\langle R \rangle = 28.6 \pm 0.2$ nm and $PDI_f = 0.026 \pm 0.005$.

An NTA experiment also gives access to the number concentration (particles/mL) of the detected NP in each bin of the distribution histogram. Summing all bins and considering the dilution factor (1/2 000 000th), $1.6 \pm 0.2 \cdot 10^{15}$ NPs/mL were detected in the formulation. Assuming spherical objects, with a radius R and a density close to 1, the total volume of detected matter by the NTA gave only about 50% of the ingredients initially introduced and supposed to participate in the LNC formation (Cap, PEG-HS, and Lip). As a control, the same procedure was applied to a polystyrene latex standard suspension with a radius close to 30 nm, which gave the correct mass balance within less than 10%. Indeed, polystyrene NPs have a refractive index $n = 1.59$, higher than for the LNCs which are mainly constituted of a Cap core ($n = 1.45$). Thus, polystyrene NPs have a brightness of around five-fold higher compared to LNCs of equivalent sizes.

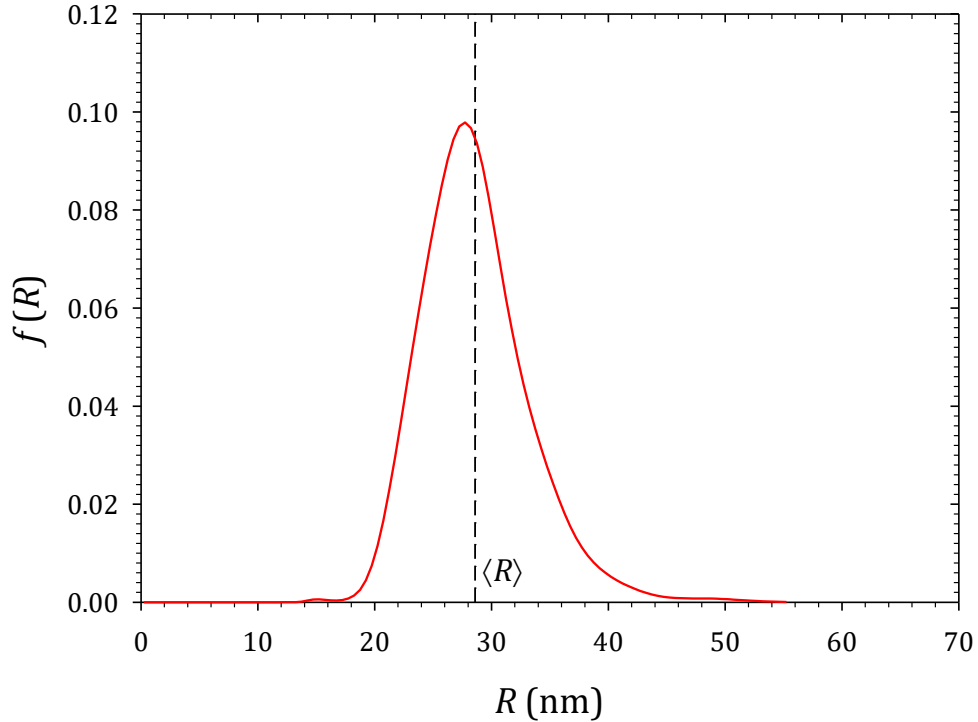


Figure 2. NTA: Number size distribution function obtained by NTA for the same NL-LNC dispersion used in **Figs. 1**. The area below the curve is normalized to 1. The black vertical dashed line depicts the corresponding number-average hydrodynamic radius $\langle R \rangle$.

This lack of detected matter could partly result from the lack of detection of the smallest LNCs but also from the presence of a non-negligible amount of residual surfactant molecules not incorporated in the LNCs. With a $1/2\,000\,000^{\text{th}}$ dilution necessary to fulfill the good operating conditions (around 10^8 NP/mL), residual surfactant molecules, if present, are necessary in the form of unimers as their concentration is much lower than the Kol CMC. Of course, they cannot be detected by NTA. Such residual surfactant molecules, in the form of residual micellar structures, has previously been revealed by DLS on a model chemical system (octaethylene glycol hexadecyl ether + hexadecane + water) using a similar formulation process [65]. They were called “wasted” micelles as they do not participate in the formation of the nanodroplets. For LNCs with similar ingredients (Kol+MCT+water) and prepared by the same formulation process used in the present paper, residual micelles were also suspected using hydrodynamic chromatography [21], but not clearly identified.

4.1.3. FRAP

FRAP experiments were performed on DiI-LNC and DiI-Kol samples for comparison. In both cases, the dilution (0.4 wt% solid content) led to systems far above the Kol CMC. **Fig. 3** shows the time evolution of the recovery ratio in the ROI, $\langle r_{\text{ROI}}(t) \rangle$, for both samples. Note that the 5 first experimental points had to be discarded to use the Kang *et al.* model (blue curves) [54] until radial

profiles had a Gaussian shape (see 2.5). This was achieved while the recovery ratio had already reached around 45 %.

For DiI-Kol, both MC and Kang approaches fit very well with experimental data. They give a hydrodynamic radius $R = 4.9 \pm 0.1$ nm and $R = 5.5 \pm 0.5$ nm respectively, confirming the presence of PEG-HS micelles in Kol sample. Both values are smaller than the one measured by SADLS. But it is not surprising as, to a first approximation, FRAP sizes correspond to volume or surface averages (depending on the location of the dye in micelles) while DLS sizes are square volume averages. Moreover, PEG-HS micelles are dynamical structures (contrary to frozen) and DiI molecules could partly diffuse from micelles to micelles, accelerating the global recovery process in the ROI.

For DiI-LNC dispersions, fits are somewhat less accurate. The MC model better adjusts short times while the Kang model is in better agreement for larger times. They give a hydrodynamic radius $R = 15.8 \pm 0.3$ nm and $R = 18.8 \pm 0.9$ nm, respectively. Both values are significantly smaller than average radii measured by DLS or NTA. As a comparison, the green curve in **Fig. 3** shows the expected recovery for NP with a 30 nm hydrodynamic radius using the MC algorithm with the initial bleached profile of the DiI-LNC sample. The fluorescence of the system is transported by objects with an average size in between micelles and LNC. Again, a non-negligible quantity of fluorescent residual micelles could explain that finding. Under this hypothesis, $\langle r_{\text{ROI}}(t) \rangle$ would result from 2 contributions: residual micellar structures and LNCs, both with 2 different kinetics, $\langle r_{\text{ROI}}(t) \rangle_{\text{micelles}}$ and $\langle r_{\text{ROI}}(t) \rangle_{\text{LNC}}$ respectively. Assuming $\langle r_{\text{ROI}}(t) \rangle_{\text{LNC}}$ and $\langle r_{\text{ROI}}(t) \rangle_{\text{micelles}}$ are described by the green solid line and the Kol red solid line, respectively (see **Fig. 3a**), the fraction f of fluorescence brought back by micelles can be estimated around $40 \pm 5\%$. **Fig 3b** shows the resulting recovery obtained using $f = 0.4$ (black solid line) with equation: $\langle r_{\text{ROI}}(t) \rangle = f \cdot \langle r_{\text{ROI}}(t) \rangle_{\text{micelles}} + (1 - f) \cdot \langle r_{\text{ROI}}(t) \rangle_{\text{LNC}}$. It is not sure that residual micellar structures have the same size as PEG-HS micelles as they could be slightly bigger if swollen with some oil [65]. But, to a first approximation, the fluorescence recovery of a DiI-LNC dispersion can be reasonably described by a linear combination of 2 contributions where residual micellar structures bring back around 40% of the fluorescence in the ROI.

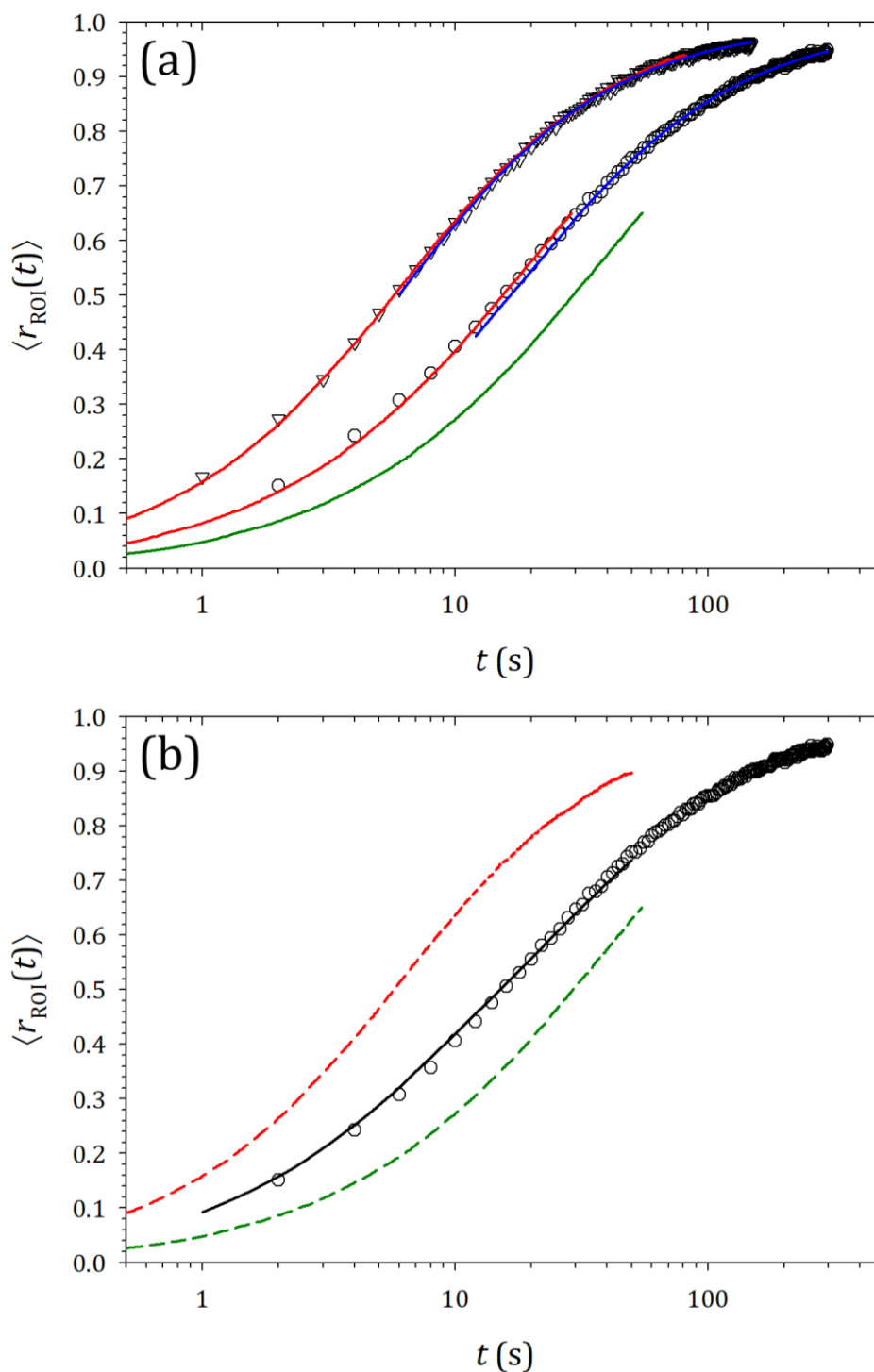


Figure 3. FRAP: Time evolution of $\langle r_{\text{ROI}}(t) \rangle$ for dilute samples (0.4 % w/v) of DiI-Kol (triangles) and DiI-LNC (circles) in water at 30°C using a 60 μm diameter ROI. (a) Full red lines are fits using the MC method and full blue lines using the Kang *et al.* model [54] where the five first experimental points had to be discarded (see text). The green full line represents the expected $\langle r_{\text{ROI}}(t) \rangle$ obtained by the MC method for NP having a hydrodynamic radius of 30 nm. (b) Recovery kinetics obtained by MC simulations are given as dashed lines for Kol micelles (red) and 30 nm radius NPs (green). The full black line represents the linear combination of both MC kinetics with a fluorescent ratio $f = 0.4$ for micelles (see text).

4.1.4. NMR diffusometry

^1H diffusometry experiments need to be performed in D_2O to get rid of the massive water proton resonance that would hide any details originating from moieties present in the dispersion. Anyhow, samples formulated in D_2O were not significantly different from that in water (see **Table 1**). Relevant ^1H NMR resonance peaks identified in D_2O are presented in **Table 2** (see **S3** for details). **Fig 4** shows a typical spectrum obtained for a D_2O -LNC dispersion with the corresponding proton peaks identified in **Table 2**. The thin peak at 4.70 ppm results from H_2O traces present in the sample. As it does not interfere with other relevant resonances, it has been discarded in the analysis. Peak A (around 5.25 ppm) corresponds to the proton resonance of the secondary hydroxyl group in the triglyceride. It is only present in Cap molecules and is well separated from others. Other peaks correspond to protons present both in Cap and PEG-HS. The large peak C corresponds to ethoxy protons, present both in free PEG chains and in PEG-HS.

From the previous findings, a 3-component SCORE analysis was carried out as three main diffusing species are suspected in a LNC formulation (i.e., free PEG chains, residual micellar structures, and LNCs). **Fig. 5** presents results obtained on D_2O -LNC samples with various solid contents. As expected, the three diffusion coefficients decrease with the concentration as steric interactions increase and hinder Brownian motions (**Fig. 5**). To calculate the corresponding hydrodynamic radii, an extrapolation to zero concentration was performed with 2nd-order polynomial fits. The results were the following: fast component $D = 221 \pm 20 \mu\text{m}^2/\text{s}$ ($R = 0.9 \pm 0.1 \text{ nm}$), medium component $D = 26 \pm 2 \mu\text{m}^2/\text{s}$ ($R = 8 \pm 1 \text{ nm}$), slow component $D = 6.2 \pm 0.1 \mu\text{m}^2/\text{s}$ ($R = 30 \pm 1 \text{ nm}$). Due to the limited number of experimental points used ($n=4$), the calculation of a confident interval for the zero extrapolated values is irrelevant and errors are expressed as standard errors. The chemical signature of each diffusing component is shown in the supplementary material section (**Fig. S4.1**). The fastest one (**Fig. S4.1b**) only involves ethoxy protons (PEG) with a hydrodynamic radius close to 1 nm. It corresponds unambiguously to the diffusion of free PEG chains in the sample. The medium one (**Fig. S4.1c**) is made of a large amount of PEG, some esters, and alkyl chains with a hydrodynamic radius close to 8 nm. It could correspond to micellar structures mainly composed of PEG-HS. No significant trace of Cap is detected around 5.2 ppm. Finally, the slow component (**Fig. S4.1d**) involves Cap, esters, alkyl chains, and some PEG. It surely corresponds to LNCs as its hydrodynamic radius is close to 30 nm. The weight of each component is very similar whatever the concentration but cannot be directly related to the molar fraction of protons in each carrier due to spin relaxation issues that generally tend to lower the contribution of the slowest particles [43,44]. As a comparison, an NMR diffusometry experiment was carried out on a D_2O -Kol solution (1 wt%) at 25°C. A 2-component SCORE analysis gave $D_s = 229 \mu\text{m}^2/\text{s}$ for the free PEG chains and $D_s = 30.5 \mu\text{m}^2/\text{s}$ for PEG-HS

micelles. This corresponds to apparent hydrodynamic radii are 0.9 nm for PEG chains and 6.5 nm for PEG-HS micelles. As no extrapolation to zero concentration was performed, apparent hydrodynamic radii could be slightly overestimated compared to real ones. Anyhow, the value obtained for PEG-HS micelles is in good agreement with DLS (**Table 1**) or FRAP results. Thus, structures with size 8 ± 1 nm present in D₂O-LNC dispersions appear significantly bigger than PEG-HS micelles (6.0 ± 0.1 nm). This is conceivable as expected “wasted” micelles are supposed to be swollen with a small amount of the oil used in the formulation [65], Cap in the present case. In **Fig. S4.1**, the signature of Cap molecules (around 5.2 ppm) is only visible in the LNC contribution, but the signal intensity is very small (only one proton per Cap molecule and probably spin relaxation issues for slow diffusing components). Some Cap could be present in micellar structures but not in sufficient quantity to be detected by NMR diffusometry.

Table 2

NMR: Chemical structures of principal ingredients used in LNC formulations. Colored letters indicate protons identified in the ¹H NMR spectrum in **Fig. 4** using same color codes.

| Name | | Chemicals with NMR peak codes (in D ₂ O) |
|-----------------------|-------------------------|--|
| Captex® 8000 (Cap) | | |
| Kolliphor® HS15 (Kol) | Mono-ester (PEG-HS1) | |
| | Di-ester (PEG-HS2) | |
| | PEG | |

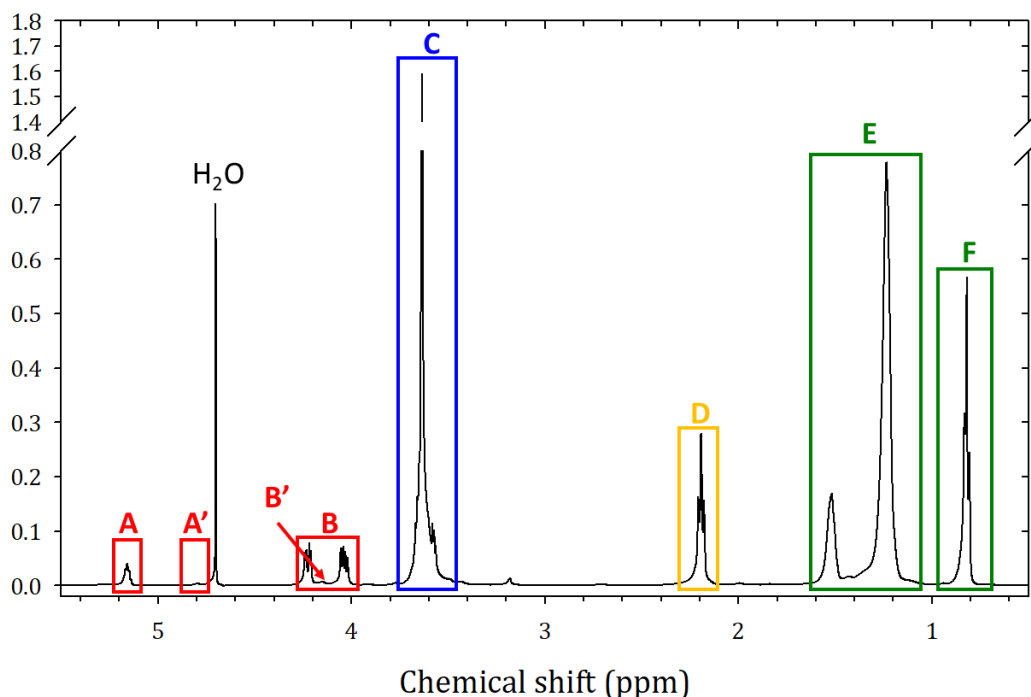


Figure 4. NMR: ^1H NMR spectrum of a typical 1 wt% D_2O -LNC dispersion. Lettered colored boxes correspond to protons identified in **Table 2** with the same color code. Y-axis breaks enable the magnification of low-intensity peaks, especially the ones that involve the resonance of very few numbers of protons per molecule like A, A', B, and B'.

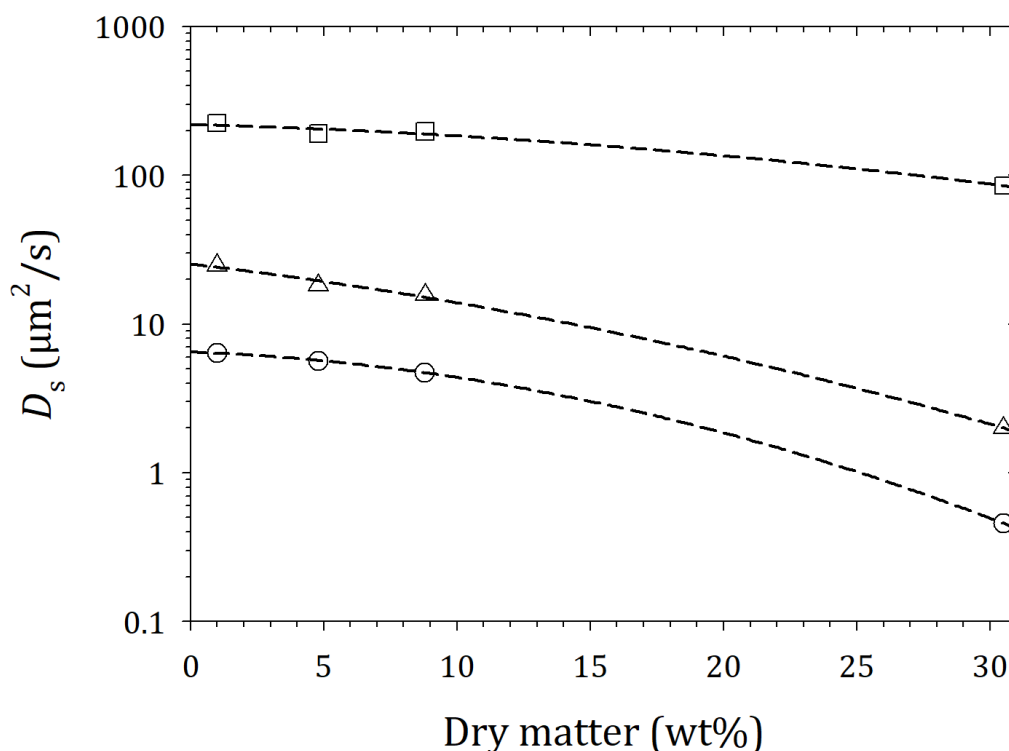


Figure 5. NMR: 3-component SCORE analysis of DOSY measurements on a D_2O -LNC dispersion at 25°C . Log-lin representation of the self-diffusion coefficients for each component (open squares: fast, open triangles: medium, open circles: slow) as a function of the solid content in the dispersion. Dashed lines show 2nd-order polynomial fits to the data (calculated on a lin-lin scale). Corresponding component contributions to the NMR signal are given in **Fig. S4.1**.

4.1.5. Ultracentrifugation of LNC dispersions

To characterize more precisely the micellar fraction present in LNC dispersions, DiI and D₂O-LNC formulations were ultra-centrifugated. After 8h at 259 000 g, no pellet was observed, and an opalescent gel-like phase was formed in the upper part of the tube (corresponding to around 50% of the volume). Below, a clearer phase occupies the residual volume (see **Fig. 6a**). The supernatant is mainly made of LNCs that have creamed as their density, close to that of Cap (0.95 g/mL), is smaller than the solvent density (H₂O, 1.00 g/mL or D₂O, 1.10 g/mL at 20°C [62]). This was confirmed by SADLS and NTA measurements on redispersed supernatants giving sizes very close to but slightly higher than that of native dispersions (around 10% by SADSL and 2% by NTA). This slight increase is likely due to redispersion issues from the gel-like state.

Due to their radius being around 4 times smaller than LNCs, the suspected micellar structures should be less sensitive to the separation. Indeed, their sedimentation velocity ($\propto R^2$) is decreased by around 16-fold while their diffusion coefficient ($\propto 1/R$) is increased by around 4-fold, thus promoting their Brownian redispersion compared to directed motions. This was checked by applying the same treatment to a DiI-Kol solution (see **Fig. 6b**). Using the same protocol as for LNC dispersions, the fluorescence intensity of the lower part of the tube was not significantly different from that of the non-centrifugated dispersion. This confirms that PEG-HS fluorescent micelles are insensitive to the ultracentrifugation step and remain homogeneously distributed in the sample water phase. It is then a reasonable assumption that it will be the same for free PEG molecules (at least 6 times smaller than micelles).

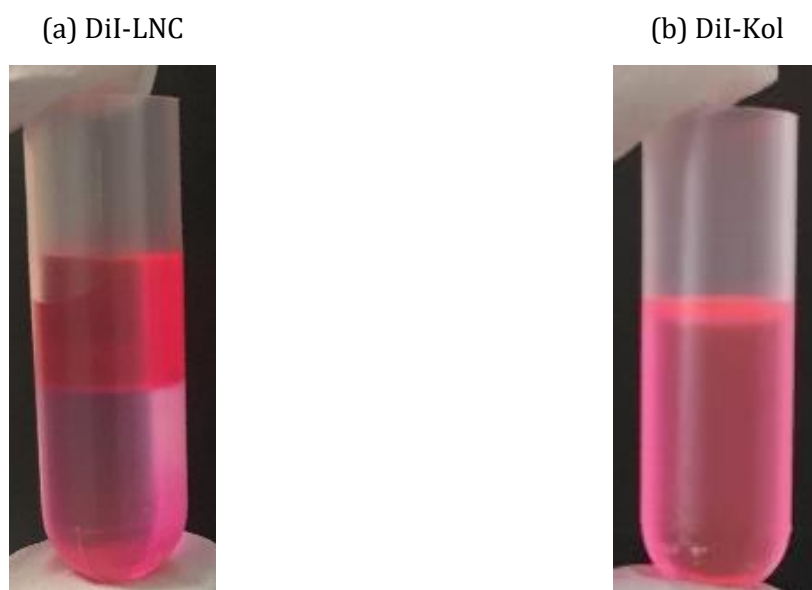


Figure 6. Ultracentrifugation: Pictures of 2.2 mL tubes after ultracentrifugation at 259 000 g for 8h. (a) The tube contains a 39 wt% dispersion of DiI-LNC in H₂O. The opalescent supernatant occupies around 50% of the volume. The clear undernatant is colored and contains a significant amount of fluorescent dye (see text). (b) The tube contains a 1 wt% aqueous solution of Kol loaded with DiI. No visual separation was observed after ultracentrifugation.

After the ultracentrifugation of DiI-LNC formulations (n=6), it was found that the fluorescence of the undernatant represents on average $44 \pm 3\%$ of the initial one. This confirms previous FRAP results in which around 40% of the fluorescence was hypothesized to account for the faster recovery curve of DiI-LNC dispersions (see **Fig. 3**).

DLS measurements were carried out at $\theta = 90^\circ$ on dilute (1/100th) undernatants (n=4) from NL-LNC and DiI-LNC dispersions. No trace of LNC was detected despite the high sensitivity of that technique to the largest particles. This demonstrates the efficacy of ultracentrifugation separation. A cumulant analysis gives $\langle 1/R \rangle_z^{-1} = 7.4 \pm 0.4$ nm with $PDI_g = 0.10 \pm 0.04$. The size is significantly bigger than that of Kol micelles (6.0 ± 0.2 nm) and very similar to the zero-concentration extrapolated value obtained by NMR diffusometry on native D₂O-LNC dispersions (8 ± 1 nm). An NMR diffusometry experiment performed on an undiluted undernatant from a D₂O-LNC dispersion and analyzed with 2-component SCORE gives $D_s = 183 \mu\text{m}^2/\text{s}$ and $D_s = 20 \mu\text{m}^2/\text{s}$ for the fast and medium components, respectively. The chemical signature of each component is shown in the supplementary material (**Fig. S4.2**). The fast one (**Fig. S4.2b**) results only from PEG protons while the medium one (**Fig. S4.2c**) also involves PEG-HS and some traces of Cap around 5.2 ppm. As the LNC component that contains the main fraction of Cap has been removed by ultracentrifugation, it is much easier to detect Cap traces in the undernatant. Self-diffusion coefficients are in good agreement with these findings and correspond to apparent hydrodynamic

radii close to 1 nm and 10 nm, for fast and medium components, respectively. Not extrapolated to zero concentration, these apparent radii are probably slightly overestimated as a non-negligible amount of solid content is present in the supernatant (see section 4.2. below). Anyhow, this unambiguously confirms the presence of residual small micellar structures in LNC formulations, mainly made of PEG-HS and swollen with a small amount of Cap.

All size measurement results have been summarized in **Table 3**, together with typical characteristics and limitations for the method used.

Table 3

Summary of results obtained from the various techniques used with their relevant characteristics.

| Technique | DLS | NTA | DOSY NMR | FRAP |
|-------------------------------------|---|---|--|---|
| Data treatment method | Cumulant [31,32] | Trajectory analysis (MSD) | SCORE with a fixed number of components [48] | Diffusion equation [54] or Monte Carlo (see S2) |
| Physical quantity obtained | Collective z-average diffusion coefficient, PDI of the relaxation rate distribution | Number distribution of self-diffusion coefficients | Self-diffusion coefficient and chemical signature of each component | Characteristic collective diffusion coefficient |
| Concentration | Low to very low | Very low | Moderate | Very low |
| Constraint | Small angle needed if optically anisotropic particles or too big and polydisperse | | Long runs needed for a good signal to noise ratio | Long runs needed to reach complete recovery if diffusion equation is used |
| Drawback | Only the biggest particles contribute (weighting factor a R^6). Very sensitive to dust | The smallest particles can elude the detection depending on their size and refractive index | Number of components must be known <i>a priori</i> . Zero concentration extrapolation needed. Spin relaxation issues to determine proton weights of each component | Polydispersity not modeled |
| Results for a LNC dispersion | $\langle 1/R \rangle_z^{-1} = 30.3 \pm 0.1$ nm $PDI_G = 0.035 \pm 0.007$ | $\langle R \rangle = 28.6 \pm 0.2$ nm $PDI_f = 0.026 \pm 0.005$ | <i>Extrapolated to zero concentration:</i> (slow component) $R = 30 \pm 1$ nm (medium component) $R = 8 \pm 1$ nm (fast component) $R = 0.9 \pm 0.1$ nm | <i>Diffusion equation:</i> $R = 18.8 \pm 0.9$ nm <i>Monte Carlo:</i> $R = 15.8 \pm 0.3$ nm |
| Results for the undernatant | $\langle 1/R \rangle_z^{-1} = 7.4 \pm 0.4$ nm $PDI_G = 0.10 \pm 0.04$ | Nothing detected | <i>At 15 wt% solid content:</i> (medium component) $R = 10$ nm (fast component) $R = 1$ nm | Not tested |
| Results for a Kol solution | $\langle 1/R \rangle_z^{-1} = 6.0 \pm 0.2$ nm $PDI_G = 0.032 \pm 0.017$ | Nothing detected | <i>At 1 wt% solid content:</i> (medium component) $R = 6.5$ nm (fast component) $R = 0.9$ nm | <i>Diffusion equation:</i> $R = 5.5 \pm 0.5$ nm <i>Monte Carlo:</i> $R = 4.9 \pm 0.1$ nm |

4.2- Distribution of ingredients in the final NP dispersion.

Previous results unambiguously demonstrate the presence of three colloidal species in LNC formulations (free short PEG chains, residual micellar structures, and LNCs).

To calculate the total amount of matter involved in the residual swollen micelles, undernatant samples were freeze-dried and weighed. The lyophilized matter also contained some NaCl and free PEG. From the quantity of sublimated water, knowing initial amounts of NaCl (2.0 mg/100 mg H₂O) and free PEG (9.0 mg/100 mg H₂O) present in a native LNC dispersion, the quantity of Cap+PEG-HS was calculated by subtraction. As the cosurfactant used (Lip) is a phospholipid, unable to form micelles (HLB<10), we assumed it was fully incorporated into LNCs and not present in residual structures having a too-small curvature radius (<10 nm). Anyhow, Lip represents less than 10 wt% of the total amount of surfactants used in the formulation. Thus, from freeze-dried samples, the amount of Cap+PEG-HS forming residual structures could be evaluated to 8.5 ± 0.2 mg/100 mg H₂O (n=3 independent formulations and 4 freeze-dried samples per formulation). Compared with the quantity of Cap+PEG-HS used in the native formulation (for a total of 51.5 mg/100 mg H₂O of which 33.0 mg of Cap and 18.5 mg of PEG-HS), around 17 wt% of the initial mass of Cap+PEG-HS were not incorporated into LNCs.

In that respect, the undernatant contains around 7 wt% of residual micelles but also around 8 wt% of free PEG chains. These non-negligible amounts (around 15 wt% in total) are certainly responsible for the overestimated hydrodynamic radii measured by NMR diffusometry on the undiluted undernatant (around 10 nm for residual micelles) due to steric hindrance compared to the zero-concentration extrapolation (8 ± 1 nm) or the DLS measurement on diluted undernatants (7.4 ± 0.4 nm), see part 4.1.5 above.

Fig. 7 shows ¹H NMR spectra in THFd of Cap, Kol, and freeze-dried undernatant. THFd was used as it is a good solvent for both blocks of PEG-HS molecules. Some resonance peaks were identified with the corresponding protons given in **Table 4** (see **S.3** for details). Peak clusters A and B (**Fig. 7a**) are specific to Cap and correspond to protons on carbon atoms close to primary and secondary esterified alcohol functions of glycerol. Peak cluster A' (**Fig. 7b**) is specific to di-ester molecules and corresponds to the proton close to the esterified alcohol function in the alkyl chain. Peak cluster B' (**Fig. 7b**) corresponds to the 2 protons on the alpha carbon of the ester group on the PEG chain side. They are found both in mono and di-ester molecules.

We clearly see that a significant amount of Cap is recovered in the undernatant (peaks A and the first quadruplet B close to 4.3 ppm in **Fig. 7c**). Thus, the signal from Cap-only molecules can easily be isolated from peak clusters A and B. Indeed, both quadruplets that compose the peak cluster B have exactly the same integrals. In the case of a mixture of Cap and PEG-HS, even if the second

quadruplet of B (close to 4.1 ppm) is superimposed with the signal B' from PEG-HS, the use of the first one (at 4.3 ppm) secures the calculation of the Cap concentration from undernatant spectra.

To calculate the amount of Cap in the undernatant, a calibration curve was established. 10 mM Maleic acid, which gives a single well-separated peak around 6.25 ppm, was used as an internal standard. Peak clusters A and B correspond to 1 and 4 protons per Cap molecule, respectively (see **Table 4**). They were used to compute S_{Cap} , a signal proportional to the number of Cap molecules. S_{Cap} is defined as the sum of peak cluster A and B integrals, normalized by the number of involved protons (five in that case), and by the integral of the maleic acid peak. The calibration curve (**Fig. S5.1**), shows the evolution of S_{Cap} as a function of the concentration of Cap. It is perfectly linear with a coefficient of determination, $r^2 = 0.9989$, and a slope of 0.102 ± 0.003 mL/mg.

Table 4

NMR: Protons identified in the 3 following compounds for ^1H NMR spectra in THFd (see **Fig. 7** with the same color codes).

| Name | Chemicals with NMR peak codes (in THFd) |
|----------------------|---|
| Captex® 8000 (Cap) | |
| Mono-ester (PEG-HS1) | |
| Di-ester (PEG-HS2) | |

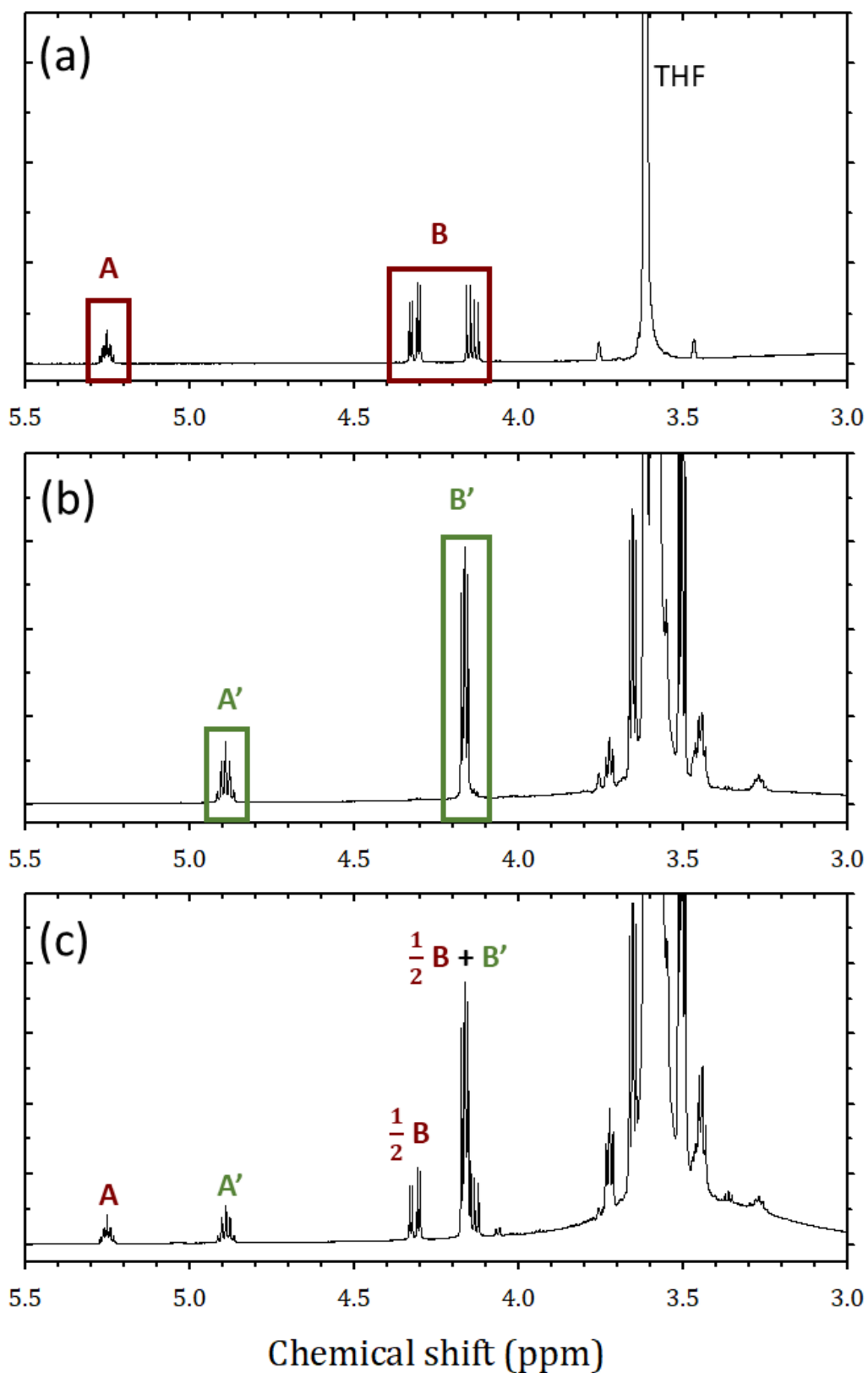
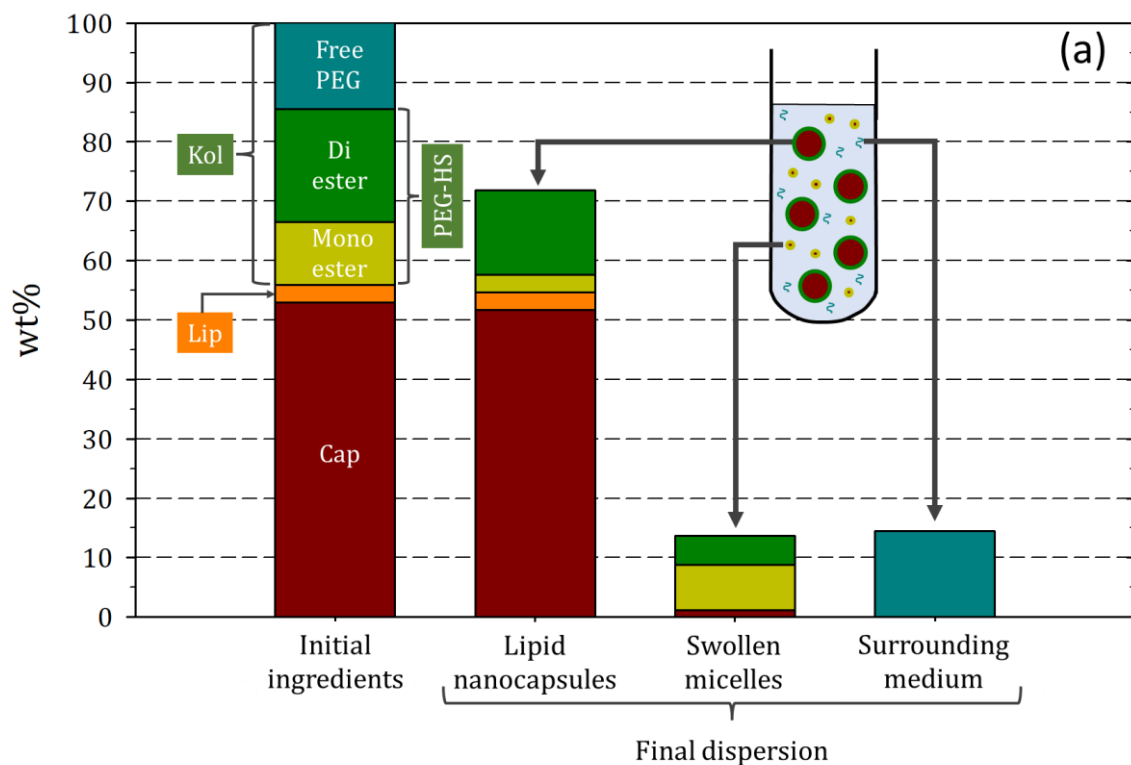


Figure 7. NMR: ^1H NMR spectra of various compounds in THFd. (a) Cap. (b) Kol. (c) Freeze-dried undernatant. Lettered colored boxes correspond to protons identified in **Table 4** with the same color code. Y-axes are in arbitrary units. Scales have been magnified to reveal relevant peaks used in the study.

From qNMR measurements on undernatants redispersed in THFd and using the established calibration curve (**Fig. S5.1**), it was found that the undernatants contained 0.74 ± 0.04 mg of Cap per 100 mg of sublimated H₂O (n=4). Thus, residual swollen micellar structures are composed of 8.6 ± 0.5 wt% of Cap and 91.4 ± 0.5 wt% of PEG-HS (n=4). This corresponds to around 2 wt% of the Cap and 42 wt% of the PEG-HS initially introduced in the formulation. The amount of PEG-HS present in residual micelles can be compared with findings from FRAP and fluorescence measurements which show that around 40 to 44 % of fluorescent dye molecules are in the residual micellar compartment. Indeed, DiI carries a positive charge and has surface-active properties [66]. Thus, it is consistent to recover DiI where the surfactant is distributed.

Finally, the distribution of mono and di-esters has been evaluated both in native Kol and in the undernatant. For pure Kol solutions, NMR signals proportional to the number of mono and di-ester molecules were easily obtained from integrals of peak clusters A' and B'. For Cap+PEG-HS mixtures, the presence of the well-separated peak clusters A' and $\frac{1}{2} \cdot B$ makes possible the calculation of the contribution of B' in the mixed peak clusters $\frac{1}{2} \cdot B+B'$ close to 4.1 ppm (see **Fig. 7c**). Using the theoretical molar masses for PEG-HS1 (961.3 Da) and PEG-HS2 (1243.7 Da), it was found that for Kol solutions, the distribution of mono/di-esters was $36:64 \pm 1$ wt% (n=4), while in the undernatant the distribution was very different. The proportion of mono-ester molecules was significantly increased with the following proportion: $61:39 \pm 1$ wt% (n=4). Monoesters are more involved in the formation of “wasted” residual micelles during the formulation process of LNCs. Consequently, the proportion of mono/di-esters in LNCs was 17:83 wt%. The tendency of monoesters to preferentially form micelles remains to be elucidated.

The distribution of all ingredients into the 3 compartments (LNCs, micelles and surrounding aqueous medium) is summarized in **Fig. 8** together with a schematic representation of the principal moieties. In that given LNC dispersion, residual micellar structures represent around 15 wt% of the solid content initially introduced while LNCs involve around 70 wt%, and free PEG chains around 15 wt%. Considering only LNCs and residual micelles, and a size ratio between both entities close to 4 (see **Table 3**), a simple calculation reveals that the contribution of residual micellar structures to the total excess scattering intensity is only around 0.3 % (see **S6** for details). This explains why those residual micellar structures cannot be detected by DLS on diluted LNC samples above the Kol CMC (1/400th). A similar calculation can be done for a Kol solution where the fraction of free PEG is around 30 wt% with a size ratio close to 6 compared to micelles. In that case, the contribution of free PEG chains to the scattering intensity can be estimated to around 0.2%. Thus, only surfactant micelles are detected by DLS and free PEG chains remain invisible.



| Name | | Schematic drawing | Colloidal assemblies (b) |
|-----------------------|----------------------|-------------------|--------------------------|
| Captex® 8000 (Cap) | | | |
| Kolliphor® HS15 (Kol) | Mono-ester (PEG-HS1) | | |
| | Di-ester (PEG-HS2) | | |
| PEG | | | |
| | | | |

Figure 8. (a) Distribution of initial ingredients in the three compartments of an LNC dispersion. (b) Schematics representation of principal moieties and their colloidal assemblies in LNC formulations.

5. Conclusion

In this study, we have unambiguously demonstrated the coexistence of residual micellar structures together with the nanodroplets when LNCs with a given composition are formulated using a given process (phase inversion in temperature followed by a quench with cold water). This confirms the results obtained by Roger et al. [65] using model chemicals, and the hypothesis formulated by Yegin and Lamprecht [21] on a very similar LNC system. The present study also highlights the strength of nuclear magnetic resonance diffusometry, the only investigation technique used capable of identifying all components in both the native LNC formulation and the LNC-free undernatant.

For the first time, a quantitative analysis was made on an LNC formulation. It was found that these micellar structures were composed of 9 wt% of medium-chain triglyceride and 91 wt% of pegylated surfactant, corresponding to around 2 wt% of the medium-chain triglyceride and 42 wt% of the pegylated surfactant initially introduced in the formulation. More specifically, the pegylated surfactant of these swollen residual micelles was mainly composed of monoesters (monoesters 61wt% and di-esters 39 wt%) while these percentages were inverted in the native Kolliphor® HS15 (36 wt% and 64 wt% respectively). Of the initial amount introduced in the formulation, around 72 wt% of the monoesters and 26 wt% of the di-esters were recovered in residual micellar structures. Now further investigations must be performed with pure mono or di-ester pegylated surfactants to determine their influence on the quantity of residual micellar structures. The influence of the surfactant-to-oil ratio (that determine the LNC average size) together with the type of formulation process must also be investigated.

LNCs are mainly proposed as a potential drug delivery system, and the existence of residual micelles raises a series of questions not addressed in the current literature, that will have to be considered in the future. Firstly, how do such micellar structures affect drug encapsulation and distribution? Indeed, in the present case, less than 60 wt% of a carbocyanine fluorescent dye was encapsulated in the LNCs. Thus, some precautions must be taken when interpreting results based on fluorescent measurements in non-clinical studies. It was demonstrated that carbocyanine dyes have more affinity for the interface than the core of LNCs [66]. So, the distribution of drugs/dyes having more affinity for the core of LNCs will have to be studied. Is the drug co-encapsulated into micellar structures and LNCs? What is the drug release profile from micellar structures vs LNCs? How is the drug protected and internalized by cells when it is either in micellar structure or LNCs? It was already demonstrated that LNCs formulated with Kolliphor® HS15 exhibit higher toxicity in HaCaT Cells in comparison to other surfactants [67], and Kolliphor® HS15 seemed to play a key role in the toxicity profile of LNCs in mouse macrophage-like cells [68]. Then, how do micellar structures affect the toxicological behavior of LNCs?

Given their use as potential drug delivery systems, the impact of such residual micelles in LNC formulations will have to be investigated in biopharmaceutical and non-clinical evaluations. Consequently, the need to control or limit their presence must be considered by improving the formulation process or developing a preparative purification method.

Declaration of Competing Interest

The authors declare that they have no known competing financial interests or personal relationships that could have appeared to influence the work reported in this paper.

Acknowledgments

Thanks to: Jérôme Béjaud, Olivier Thomas for their technical support and Dr. Jérémie Riou for his advice for the statistical analysis of FRAP results. Thanks to the Foundation Pierre Fabre for its financial support for the student mobility of T. A. T. Do in the framework of the « Master Mekong Pharma ».

CRedit author statement

E. Roger: Methodology, Validation, Investigation, Writing – Original Draft, Writing – Review & Editing.

F. Franconi: Methodology, Software, Investigation, Writing – Original Draft, Writing – Review & Editing, Visualization.

T.A.T. Do: Investigation, Writing – Review & Editing, Visualization.

C. Simonsson: Methodology, Software, Writing – Review & Editing.

B. Siegler: NMR Investigation, Methodology, Writing – Review & Editing.

R. Perrot: FRAP Investigation, Methodology, Writing – Review & Editing.

P. Saulnier: Conceptualization, Writing – Review & Editing, Funding acquisition.

J.-C. Gimel: Conceptualization, Methodology, Software, Validation, Investigation, Writing – Original Draft, Writing – Review & Editing, Visualization, Supervision.

Bibliography

- [1] J.-B. Coty, C. Vauthier, Characterization of nanomedicines: A reflection on a field under construction needed for clinical translation success, *J. Control. Release.* 275 (2018) 254–268. doi:10.1016/j.jconrel.2018.02.013.
- [2] F. Farjadian, A. Ghasemi, O. Gohari, A. Roointan, M. Karimi, M.R. Hamblin, Nanopharmaceuticals and nanomedicines currently on the market: challenges and opportunities, *Nanomedicine.* 14 (2019) 93–126. doi:10.2217/nmm-2018-0120.
- [3] C. Hald Albertsen, J.A. Kulkarni, D. Witzigmann, M. Lind, K. Petersson, J.B. Simonsen, The role of lipid components in lipid nanoparticles for vaccines and gene therapy, *Adv. Drug Deliv. Rev.* 188 (2022) 114416. doi:10.1016/j.addr.2022.114416.
- [4] N. Bertrand, J.-C. Leroux, The journey of a drug-carrier in the body: An anatomophysiological perspective, *J. Control. Release.* 161 (2012) 152–163. doi:10.1016/j.jconrel.2011.09.098.
- [5] S. Gioria, F. Caputo, P. Urbán, C.M. Maguire, S. Bremer-Hoffmann, A. Prina-Mello, L. Calzolari, D. Mehn, Are existing standard methods suitable for the evaluation of nanomedicines: Some case studies, *Nanomedicine.* 13 (2018) 539–554. doi:10.2217/nmm-2017-0338.
- [6] F. Caputo, J. Clogston, L. Calzolari, M. Rösslein, A. Prina-Mello, Measuring particle size distribution of nanoparticle enabled medicinal products, the joint view of EUNCL and NCI-NCL. A step by step approach combining orthogonal measurements with increasing complexity, *J. Control. Release.* 299 (2019) 31–43. doi:10.1016/j.jconrel.2019.02.030.
- [7] F. Caputo, A. Arnould, M. Bacia, W.L. Ling, E. Rustique, I. Texier, A.P. Mello, A.C. Couffin, Measuring Particle Size Distribution by Asymmetric Flow Field Flow Fractionation: A Powerful Method for the Preclinical Characterization of Lipid-Based Nanoparticles, *Mol. Pharm.* 16 (2019) 756–767. doi:10.1021/acs.molpharmaceut.8b01033.
- [8] F. Caputo, D. Mehn, J.D. Clogston, M. Rösslein, A. Prina-Mello, S.E. Borgos, S. Gioria, L. Calzolari, Asymmetric-flow field-flow fractionation for measuring particle size, drug loading and (in)stability of nanopharmaceuticals. The joint view of European Union Nanomedicine Characterization Laboratory and National Cancer Institute - Nanotechnology Character, *J. Chromatogr. A.* 1635 (2021). doi:10.1016/j.chroma.2020.461767.

- [9] A. Zabeo, F. Rosada, L. Pizzol, F. Caputo, S.E. Borgos, J. Parot, R.E. Geertsma, J.J. Pouw, R.J. Vandebriel, O.I. Moreno, D. Hristozov, A Decision Support System for preclinical assessment of nanomaterials in medical products: the REFINE DSS, *Drug Deliv. Transl. Res.* 12 (2022) 2101–2113. doi:10.1007/s13346-022-01145-2.
- [10] C.G. Simon, S.E. Borgos, L. Calzolari, B.C. Nelson, J. Parot, E.J. Petersen, M. Roesslein, X. Xu, F. Caputo, Orthogonal and complementary measurements of properties of drug products containing nanomaterials, *J. Control. Release.* 354 (2023) 120–127. doi:10.1016/j.jconrel.2022.12.049.
- [11] N.T. Huynh, C. Passirani, P. Saulnier, J.P. Benoit, Lipid nanocapsules: A new platform for nanomedicine, *Int. J. Pharm.* 379 (2009) 201–209. doi:10.1016/j.ijpharm.2009.04.026.
- [12] B. Heurtault, P. Saulnier, B. Pech, J.-E. Proust, J.-P. Benoit, A novel phase inversion-based process for the preparation of lipid nanocarriers, *Pharm. Res.* 19 (2002) 875–880. doi:10.1023/A:1016121319668.
- [13] B. Heurtault, P. Saulnier, B. Pech, M.-C. Venier-Julienne, J.-E. Proust, R. Phan-Tan-Luu, J.-P. Benoît, The influence of lipid nanocapsule composition on their size distribution, *Eur. J. Pharm. Sci.* 18 (2003) 55–61. doi:10.1016/S0928-0987(02)00241-5.
- [14] E. Roger, F. Lagarce, E. Garcion, J.-P. Benoit, Lipid nanocarriers improve paclitaxel transport throughout human intestinal epithelial cells by using vesicle-mediated transcytosis, *J. Control. Release.* 140 (2009) 174–181. doi:10.1016/j.jconrel.2009.08.010.
- [15] Y. Xu, D. Carradori, M. Alhouayek, G.G. Muccioli, P.D. Cani, V. Pr eat, A. Beloqui, Size Effect on Lipid Nanocapsule-Mediated GLP-1 Secretion from Enteroendocrine L Cells, *Mol. Pharm.* 15 (2018) 108–115. doi:10.1021/acs.molpharmaceut.7b00742.
- [16] O. Thomas, F. Lagarce, Lipid nanocapsules: A nanocarrier suitable for scale-up process, *J. Drug Deliv. Sci. Technol.* 23 (2013) 555–559. doi:10.1016/S1773-2247(13)50084-0.
- [17] F. Lagarce, C. Passirani, Nucleic-Acid Delivery Using Lipid Nanocapsules, *Curr. Pharm. Biotechnol.* 17 (2016) 723–727. doi:10.2174/1389201017666160401145206.
- [18] B. Le Moal,  . Lepeltier, D. Rouleau, C. Le Visage, J.-P. Benoit, C. Passirani, J. Guicheux, M. Fusellier, J. Clouet, Lipid nanocapsules for intracellular delivery of microRNA: A first step towards intervertebral disc degeneration therapy, *Int. J. Pharm.* 624 (2022) 121941. doi:10.1016/j.ijpharm.2022.121941.

- [19] J.S. Komaiko, D.J. McClements, Formation of Food-Grade Nanoemulsions Using Low-Energy Preparation Methods: A Review of Available Methods, *Compr. Rev. Food Sci. Food Saf.* 15 (2016) 331–352. doi:10.1111/1541-4337.12189.
- [20] A. Gupta, H.B. Eral, T.A. Hatton, P.S. Doyle, Nanoemulsions: Formation, properties and applications, *Soft Matter.* 12 (2016) 2826–2841. doi:10.1039/c5sm02958a.
- [21] B. Yegin, A. Lamprecht, Lipid nanocapsule size analysis by hydrodynamic chromatography and photon correlation spectroscopy, *Int. J. Pharm.* 320 (2006) 165–170. doi:10.1016/j.ijpharm.2006.04.014.
- [22] K. Roger, Nanoemulsification in the vicinity of phase inversion: Disruption of bicontinuous structures in oil/surfactant/water systems, *Curr. Opin. Colloid Interface Sci.* 25 (2016) 120–128. doi:10.1016/j.cocis.2016.09.015.
- [23] L. Guyon, E. Lepeltier, J.-C. Gimel, B. Calvignac, F. Franconi, N. Lautram, A. Dupont, C. Bourgaux, P. Pigeon, P. Saulnier, G. Jaouen, C. Passirani, Importance of Combining Advanced Particle Size Analysis Techniques To Characterize Cell-Penetrating Peptide-Ferrocifen Self-Assemblies, *J. Phys. Chem. Lett.* (2019) 6613–6620. doi:10.1021/acs.jpcllett.9b01493.
- [24] J.K.G. Dhont, *Introduction to Dynamics of Colloids*, 2nd ed., Elsevier, Amsterdam, 1996.
- [25] M. Tokuyama, I. Oppenheim, Dynamics of hard-sphere suspensions, *Phys. Rev. E.* 50 (1994) R16–R19. doi:10.1103/PhysRevE.50.R16.
- [26] W.R. Bowen, A. Mongruel, Calculation of the collective diffusion coefficient of electrostatically stabilised colloidal particles, *Colloids Surfaces A Physicochem. Eng. Asp.* 138 (1998) 161–172. doi:10.1016/S0927-7757(96)03954-4.
- [27] B. Chu, *Laser Light Scattering*, *Annu. Rev. Phys. Chem.* 21 (1970) 145–174. doi:10.1146/annurev.pc.21.100170.001045.
- [28] K. Fischer, M. Schmidt, Pitfalls and novel applications of particle sizing by dynamic light scattering, *Biomaterials.* 98 (2016) 79–91. doi:10.1016/j.biomaterials.2016.05.003.
- [29] B.J. Berne, R. Pecora, *Dynamic Light Scattering: With Applications to Chemistry, Biology, and Physics*, Dover Publications Inc., Mineola, 2003.
- [30] O. Glatter, *Scattering Methods and their Application in Colloid and Interface Science*, Elsevier, Amsterdam, 2018. doi:10.1016/C2016-0-04640-5.

- [31] D.E. Koppel, Analysis of macromolecular polydispersity in intensity correlation spectroscopy: The method of cumulants, *J. Chem. Phys.* 57 (1972) 4814–4820. doi:10.1063/1.1678153.
- [32] B.J. Frisken, Revisiting the method of cumulants for the analysis of dynamic light-scattering data, *Appl. Opt.* 40 (2001) 4087. doi:10.1364/AO.40.004087.
- [33] P. Rainer, Noise on photon correlation functions and its effect on data reduction algorithms, in: W. Brown (Ed.), *Dyn. Light Scatt. Method Some Appl.*, Clarendon Press, Oxford, 1993: pp. 149–176.
- [34] J. Jakeš, Regularized Positive Exponential Sum (REPES) Program - A Way of Inverting Laplace Transform Data Obtained by Dynamic Light Scattering, *Collect. Czechoslov. Chem. Commun.* 60 (1995) 1781–1797. doi:10.1135/cccc19951781.
- [35] S.W. Provencher, A constrained regularization method for inverting data represented by linear algebraic or integral equations, *Comput. Phys. Commun.* 27 (1982) 213–227. doi:10.1016/0010-4655(82)90173-4.
- [36] S.-L. Nyeo, R.R. Ansari, Sparse Bayesian learning for the Laplace transform inversion in dynamic light scattering, *J. Comput. Appl. Math.* 235 (2011) 2861–2872. doi:10.1016/j.cam.2010.12.008.
- [37] LS Instruments, DLS Data Analysis: The CORENN Method, (n.d.). <https://lsinstruments.ch/en/theory/dynamic-light-scattering-dls/dls-data-analysis-the-corenn-method> (accessed June 19, 2023).
- [38] S. Schintke, E. Frau, Modulated 3d cross-correlation dynamic light scattering applications for optical biosensing and time-dependent monitoring of nanoparticle-biofluid interactions, *Appl. Sci.* 10 (2020) 1–11. doi:10.3390/app10248969.
- [39] B. Carr, P. Hole, A. Malloy, P. Nelson, M. Wright, J. Smith, M. Park, Applications of nanoparticle tracking analysis in nanoparticle research – a mini-review, *Eur. J. Parenter. Pharm. Sci.* 14 (2009) 45–50.
- [40] V. Filipe, A. Hawe, W. Jiskoot, Critical evaluation of nanoparticle tracking analysis (NTA) by NanoSight for the measurement of nanoparticles and protein aggregates, *Pharm. Res.* 27 (2010) 796–810. doi:10.1007/s11095-010-0073-2.

- [41] E.O. Stejskal, J.E. Tanner, Spin diffusion measurements: Spin echoes in the presence of a time-dependent field gradient, *J. Chem. Phys.* 42 (1965) 288–292.
doi:10.1063/1.1695690.
- [42] A.S. Altieri, D.P. Hinton, R.A. Byrd, Association of Biomolecular Systems via Pulsed Field Gradient NMR Self-Diffusion Measurements, *J. Am. Chem. Soc.* 117 (1995) 7566–7567.
doi:10.1021/ja00133a039.
- [43] B. Antalek, Accounting for Spin Relaxation in Quantitative Pulse Gradient Spin Echo NMR Mixture Analysis, *J. Am. Chem. Soc.* 128 (2006) 8402–8403. doi:10.1021/ja062592c.
- [44] C. Barrère, P. Thureau, A. Thévand, S. Viel, Acquisition strategy to obtain quantitative diffusion NMR data, *J. Magn. Reson.* 216 (2012) 201–208. doi:10.1016/j.jmr.2011.12.022.
- [45] F. Franconi, L. Lemaire, B. Siegler, J.-C. Gimel, P. Saulnier, NMR diffusometry data sampling optimization for mixture analysis, *J. Pharm. Biomed. Anal.* 148 (2018).
doi:10.1016/j.jpba.2017.09.028.
- [46] P. Stilbs, K. Paulsen, P.C. Griffiths, Global Least-Squares Analysis of Large, Correlated Spectral Data Sets: Application to Component-Resolved FT-PGSE NMR Spectroscopy, *J. Phys. Chem.* 100 (1996) 8180–8189. doi:10.1021/jp9535607.
- [47] W. Windig, B. Antalek, Direct exponential curve resolution algorithm (DECRA): A novel application of the generalized rank annihilation method for a single spectral mixture data set with exponentially decaying contribution profiles, *Chemom. Intell. Lab. Syst.* 37 (1997) 241–254. doi:10.1016/S0169-7439(97)00028-2.
- [48] M. Nilsson, G.A. Morris, Speedy Component Resolution: An Improved Tool for Processing Diffusion-Ordered Spectroscopy Data, *Anal. Chem.* 80 (2008) 3777–3782.
doi:10.1021/ac7025833.
- [49] D. Axelrod, D.E. Koppel, J. Schlessinger, E. Elson, W.W. Webb, Mobility measurement by analysis of fluorescence photobleaching recovery kinetics, *Biophys. J.* 16 (1976) 1055–1069. doi:10.1016/S0006-3495(76)85755-4.
- [50] D.E. Koppel, D. Axelrod, J. Schlessinger, E.L. Elson, W.W. Webb, Dynamics of fluorescence marker concentration as a probe of mobility, *Biophys. J.* 16 (1976) 1315–1329.
doi:10.1016/S0006-3495(76)85776-1.

- [51] J.C.G. Blonk, A. Don, H. Van Aalst, J.J. Birmingham, Fluorescence photobleaching recovery in the confocal scanning light microscope, *J. Microsc.* 169 (1993) 363–374. doi:10.1111/j.1365-2818.1993.tb03312.x.
- [52] N. Lorén, J. Hagman, J.K. Jonasson, H. Deschout, D. Bernin, F. Cella-Zanacchi, A. Diaspro, J.G. McNally, M. Ameloot, N. Smisdom, M. Nydén, A.M. Hermansson, M. Rudemo, K. Braeckmans, Fluorescence recovery after photobleaching in material and life sciences: Putting theory into practice, *Q. Rev. Biophys.* 48 (2015) 323–387. doi:10.1017/S0033583515000013.
- [53] J. Crank, *The Mathematics of Diffusion*, 2nd ed., Clarendon Press, Oxford, 1975.
- [54] M. Kang, C.A. Day, K. Drake, A.K. Kenworthy, E. DiBenedetto, A Generalization of Theory for Two-Dimensional Fluorescence Recovery after Photobleaching Applicable to Confocal Laser Scanning Microscopes, *Biophys. J.* 97 (2009) 1501–1511. doi:10.1016/j.bpj.2009.06.017.
- [55] J.K. Jonasson, N. Lorén, P. Olofsson, M. Nydén, M. Rudemo, A pixel-based likelihood framework for analysis of fluorescence recovery after photobleaching data, *J. Microsc.* 232 (2008) 260–269. doi:10.1111/j.1365-2818.2008.02097.x.
- [56] J.K. Jonasson, J. Hagman, N. Lorén, D. Bernin, M. Nydén, M. Rudemo, Pixel-based analysis of FRAP data with a general initial bleaching profile, *J. Microsc.* (2010). doi:10.1111/j.1365-2818.2009.03361.x.
- [57] D. Blumenthal, L. Goldstien, M. Edidin, L.A. Gheber, Universal approach to FRAP analysis of arbitrary bleaching patterns, *Sci. Rep.* 5 (2015) 1–9. doi:10.1038/srep11655.
- [58] P. Jönsson, M.P. Jonsson, J.O. Tegenfeldt, F. Höök, A Method Improving the Accuracy of Fluorescence Recovery after Photobleaching Analysis, *Biophys. J.* 95 (2008) 5334–5348. doi:10.1529/biophysj.108.134874.
- [59] BASF, Kolliphor® HS 15, Technical Information, (2020) 1–5. <https://pharma.basf.com/technicalinformation/30554050/kolliphor-hs-15>.
- [60] D.H. Bae, J.S. Shin, F.L. Jin, G.S. Shin, S.J. Park, Effect of hydrogenated lecithin on cytotoxicity of liposome, *Bull. Korean Chem. Soc.* 30 (2009) 339–342. doi:10.5012/bkcs.2009.30.2.339.

- [61] N. Kaeokhamloed, E. Roger, J. Béjaud, N. Lautram, F. Manero, R. Perrot, M. Briet, C. Abbara, S. Legeay, New In Vitro Coculture Model for Evaluating Intestinal Absorption of Different Lipid Nanocapsules, *Pharmaceutics*. 13 (2021) 595.
doi:10.3390/pharmaceutics13050595.
- [62] F.J. Millero, R. Dexter, E. Hoff, Density and viscosity of deuterium oxide solutions from 5-70.deg., *J. Chem. Eng. Data*. 16 (1971) 85–87. doi:10.1021/je60048a006.
- [63] L. Korson, W. Drost-Hansen, F.J. Millero, Viscosity of water at various temperatures, *J. Phys. Chem.* 73 (1969) 34–39. doi:10.1021/j100721a006.
- [64] F.D. Gunstone, J.L. Harwood, J.L. Harwood, eds., *The Lipid Handbook*, 3rd ed., CRC Press, Boca Raton, 2007. doi:10.1201/9781420009675.
- [65] K. Roger, B. Cabane, U. Olsson, Emulsification through Surfactant Hydration: The PIC Process Revisited, *Langmuir*. 27 (2011) 604–611. doi:10.1021/la1042603.
- [66] G. Bastiat, C.O. Pritz, C. Roider, F. Fouchet, E. Lignières, A. Jesacher, R. Glueckert, M. Ritsch-Marte, A. Schrott-Fischer, P. Saulnier, J.-P. Benoit, A new tool to ensure the fluorescent dye labeling stability of nanocarriers: A real challenge for fluorescence imaging, *J. Control. Release*. 170 (2013) 334–342. doi:10.1016/j.jconrel.2013.06.014.
- [67] C. Maupas, B. Moulari, A. Béduneau, A. Lamprecht, Y. Pellequer, Surfactant dependent toxicity of lipid nanocapsules in HaCaT cells, *Int. J. Pharm.* 411 (2011) 136–141.
doi:10.1016/j.ijpharm.2011.03.056.
- [68] G. Le Roux, H. Moche, A. Nieto, J.P. Benoit, F. Nessler, F. Lagarce, Cytotoxicity and genotoxicity of lipid nanocapsules, *Toxicol. Vitro*. 41 (2017) 189–199.
doi:10.1016/j.tiv.2017.03.007.

Supplementary material:

Evidence of residual micellar structures in a lipid nanocapsule dispersion. A multi-technique approach.

Emilie ROGER^(a), Florence FRANCONI^{(a)(b)}, Tran Anh Thu DO^(a), Carl SIMONSSON^(a), Benjamin SIEGLER^(c), Rodolphe PERROT^(d), Patrick SAULNIER^(a), Jean-Christophe GIMEL^{(a)(*)}

(a) **Univ Angers**, Inserm, CNRS, **MINT**, SFR ICAT, F-49000 Angers, France

(b) **Univ Angers**, **PRISM**, SFR ICAT, Biogenouest F-49000 Angers, France

(c) **Univ Angers**, **ASTRAL**, SFR MATRIX, F-49000 Angers, France

(d) **Univ Angers**, **SCIAM**, SFR ICAT, F-49000 Angers, France

(*) Corresponding author: jean-christophe.gimel@univ-angers.fr, Tel: +33 2 4468 8529, Fax +33 2 4468 8546. Lab MINT, IBS-CHU, 4 rue Larrey, F-49933, Angers cedex, France.

List of symbols

| | |
|-----------------------|---|
| $A(\tau)$ | Distribution function of relaxation times of the electric field-time correlation function |
| α | size ratio in a binary spherical NP dispersion |
| β | Fraction of the excess intensity scattered by small NPs (type 1) in a binary mixture of spherical NPs |
| D | Translational diffusion coefficient of a nanoparticle in dilute conditions in a simple liquid |
| D_c | Collective diffusion coefficient of a nanoparticle |
| D_s | Self diffusion coefficient of a nanoparticle |
| $\langle D \rangle_z$ | z-average translational diffusion coefficient |

| | |
|--------------------------|---|
| Δt | Delay time of correlation functions |
| f_m | Mass fraction of the small NPs (type 1) in a binary mixture of spherical NPs |
| $f(R)$ | Number-size distribution function of nanoparticle with hydrodynamic radii R |
| $g_1(q, \Delta t)$ | Electric field-time correlation function of the scattered light at diffusion vector q and delay time Δt |
| $g_2(q, \Delta t)$ | Intensity-time correlation function of the scattered light at diffusion vector q and delay time Δt |
| $G(\Gamma)$ | Distribution function of relaxation rates Γ of the electric field-time correlation function |
| Γ | Relaxation rate |
| $\langle \Gamma \rangle$ | Average relaxation rate of $G(\Gamma)$, also called first cumulant |
| η | Viscosity of the solvent |
| I_0 | Average fluorescence intensity in the sample before bleaching |
| $I(\mathbf{r}, t)$ | Fluorescence intensity at position \mathbf{r} and time t in the region of interest |
| $I_{\text{ROI}}(t)$ | Average fluorescence intensity in the region of interest at time t |
| I_1 | Excess intensity scattered by one type 1 NP |
| I_2 | Excess intensity scattered by one type 2 NP |
| \mathbf{k}_i | Incident wave vector |
| \mathbf{k}_s | Scattered wave vector |
| I_{tot} | Total excess scattering intensity by a binary mixture of spherical NPs |
| l | linear size of a pixel |
| λ_0 | Wavelength of the incident vertically polarized laser beam |
| m_1 | Mass of type 1 spheres in a binary mixture |
| m_2 | Mass of type 2 spheres in a binary mixture |
| N | Average number of NPs in a pixel at thermal equilibrium |
| N_1 | Number of type 1 spheres in a binary mixture |

| | |
|------------------------------|---|
| N_2 | Number of type 2 spheres in a binary mixture |
| v_A | Variance of $A(\tau)$ |
| v_G | Variance of $G(\Gamma)$ |
| PDI_A | Polydispersity index of $A(\tau)$ |
| PDI_G | Polydispersity index of $G(\Gamma)$ |
| PDI^* | Polydispersity index calculated from the ratio of $\langle R \rangle_z$ by $\langle 1/R \rangle_z^{-1}$ |
| \mathbf{q} | Scattering vector |
| q | Amplitude of the scattering vector |
| θ | Scattering angle |
| r | Distance to the center of the region of interest |
| R | Hydrodynamic radius of a nanoparticle |
| $\langle R \rangle$ | Number-average hydrodynamic radius |
| R_1 | Radius of type 1 spheres in a binary mixture |
| R_2 | Radius of type 2 spheres in a binary mixture |
| $\langle R^k \rangle$ | k^{th} -order moment of $f(R)$ |
| $\langle R \rangle_z$ | z-average hydrodynamic radius calculated from $A(\tau)$ |
| $\langle 1/R \rangle_z^{-1}$ | Average hydrodynamic radius extracted from $G(\Gamma)$ |
| t | Time |
| t_0 | Time needed for a particle to jump into a neighbor pixel |
| t_{MC} | Monte Carlo time |
| T | Absolute temperature of the solvent |
| τ | Relaxation time |

List of abbreviations

| | |
|-------|---|
| Cap | Captex® 8000, glyceryl tricaprilate |
| CMC | Critical micellar concentration |
| COSY | Correlation spectroscopy |
| DiI | 1,1'-dioctadecyl-3,3,3',3'-tetra methylindocarbocyanine perchlorate |
| DLS | Dynamic light scattering |
| DOSY | Diffusion ordered spectroscopy |
| FRAP | Fluorescence recovery after photobleaching |
| HMBC | Heteronuclear multiple bond correlation |
| HSQC | Heteronuclear single quantum coherence |
| Kol | Kolliphor® HS15 |
| LNC | Lipid nanocapsule |
| MC | Monte Carlo |
| NMR | Nuclear magnetic resonance |
| NP | Nanoparticle |
| PEG | Polyethylene glycol |
| qNMR | Quantitative nuclear magnetic resonance |
| ROI | Region of interest |
| SADLS | Single-angle dynamic light scattering |

S1. Dynamic light scattering theory applied to NP dispersions

Illuminating a nanoparticle dispersion with a polarized laser beam (wavelength λ_0), dynamic light scattering (DLS) measures the intensity-time correlation function of the scattering intensity, g_2 , at a given scattering angle θ . The scattering vector, \mathbf{q} , is defined as the difference between the incident, \mathbf{k}_i , and \mathbf{k}_s , the scattered wave vectors. Its amplitude, q , is given by $q = (4\pi \cdot n)/\lambda_0 \cdot \sin(\theta/2)$, with n the refractive index of the solvent ($n = 1.33$ for water).

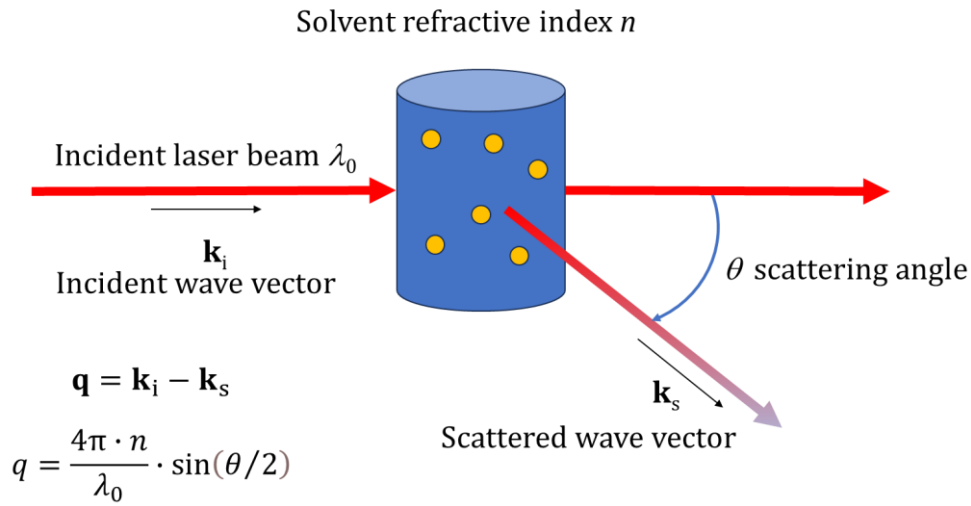


Figure S1.1. Geometry of a light scattering experiment.

Its inverse, q^{-1} , defines the characteristic length scale at which sample dynamics are probed. Assuming a Gaussian statistic for the amplitude of the scattering electric field, g_2 is related to the electric field-time correlation function, g_1 , by the so-called Siegert relation [1]: $g_2(q, \Delta t) = 1 + g_1(q, \Delta t)^2$, with Δt the delay time. Assuming no multiple scattering nor fluorescence emission then, at small q and at thermal equilibrium, scattering light fluctuations originate only from the NP concentration fluctuations in the sample.

These concentration fluctuations obey the macroscopic diffusion equation [2], thus for a dilute suspension of monodisperse NPs with size small compared to q^{-1} , it can be shown that g_1 is a simple exponential decay of Δt [1] given by **Eq. (S1.1)**. Its decay rate Γ or equivalently its relaxation time τ are related to D , the translational diffusion coefficient and the following relation is established: $\Gamma = 1/\tau = D \cdot q^2$. Strictly speaking, as the diffusion equation has been used to model NP concentration fluctuations, the derivation of **Eq. (S1.1)** involves the collective diffusion coefficient D_c and not the self-diffusion coefficient D_s of particles [3]. In the limit of a dilute NP dispersion $D_c = D_s = D$, but they have very different behaviors as the concentration is increased.

D_s is always a decreasing function of the NP concentration while D_c can first increase and then decrease with the concentration depending on the type of interparticle interactions [4,5].

$$g_1(q \rightarrow 0, \Delta t) = \exp(-\Gamma \cdot \Delta t) = \exp(-\Delta t/\tau) \quad (\text{S1.1})$$

Under these conditions, NPs are observed as independent Brownian scatterers. They decorrelate the signal in a delay time proportional to τ (the characteristic time needed to diffuse over a square distance proportional to q^{-2}). From D , knowing the absolute temperature T and the solvent viscosity η , the NP hydrodynamic radius, R , can be calculated using the Stokes-Einstein relation: $R = (k_B \cdot T)/(6\pi \cdot \eta \cdot D)$, with k_B the Boltzmann constant. The dilute condition is necessary to avoid optical and steric interactions between particles that could bias the calculation of R . For non-rigid objects like polymers, or optically anisotropic particles like rods or crystalline spheres [6], faster modes arise at higher q as internal dynamics are probed: Rouse modes [7] for polymers and rotational diffusion [8] for anisotropic particles. Therefore, g_1 becomes a multi exponential decay and a monodisperse sample can be wrongly interpreted as polydisperse with an overestimated diffusion coefficient (underestimated hydrodynamic radius), especially when single-angle measurements are performed at large angles.

The main drawback of DLS is its extreme sensitivity to biggest particles making its use tricky for characterizing polydisperse or dusty samples. Considering a distribution of nanoparticles with same refractive index, in the limit of small scattering vector (q^{-1} bigger than the biggest nanoparticle size) the contribution of each NP to the scattering intensity is proportional to the square of its volume ($\propto R^6$) [9]. Thus, NPs with ten-time bigger size weight a million time more in the scattering at small q ! In the polydisperse case, even for rigid isotropic objects, the constraint q^{-1} bigger than the biggest particle size is mandatory. It allows to ignore the form factor of the particles that could attenuate the R^6 weighting factor of the biggest [6]. This is a serious drawback for SADLS apparatus, especially when using a backscattering detector ($\theta = 173^\circ$) to probe very polydisperse NP suspensions with sizes bigger than about 100 nm. It often leads to underestimate real average sizes by lowering the contribution of the largest particles, but it also biases the determination of the sample polydispersity. This was already pointed out by Fisher and Schmidt [6].

For a polydisperse NP suspension, **Eq. (S1.1)** turns into **Eq. (S1.2)** where each NP contributes with an exponential decay to the overall relaxation. It involves equivalently $G(\Gamma)$, the distribution function of decay rates, or $A(\tau)$ the distribution of relaxation times, both distributions being simply related by: $\Gamma \cdot G(\Gamma) = \tau \cdot A(\tau)$.

$$g_1(q, \Delta t) = \int_0^\infty G(\Gamma) \cdot \exp(-\Gamma \cdot \Delta t) \cdot d\Gamma = \int_0^\infty A(\tau) \cdot \exp(-\Delta t/\tau) \cdot d\tau \quad (\text{S1.2})$$

In the low- q limit, and for a dilute suspension of spherical nanoparticles with various hydrodynamic radii R and same refractive index, $g_1(t)$ can be related to the number distribution of the radii, $f(R)$, through **Eq. (S1.3)**. Here, each NP contributes to the relaxation process with a weight proportional to its square volume. In the following, the various moments of $f(R)$ will be written as $\langle R^k \rangle = \int_0^\infty R^k \cdot f(R) \cdot dR$.

$$g_1(q \rightarrow 0, \Delta t) = \frac{1}{\langle R^6 \rangle} \cdot \int_0^\infty R^6 \cdot f(R) \cdot \exp\left(-\frac{k_B \cdot T}{6\pi \cdot \eta \cdot R} \cdot q^2 \cdot \Delta t\right) \cdot dR \quad (\text{S1.3})$$

Then, identifying **Eq (S1.2)** to **Eq. (S1.3)**, gives the relation between $G(\Gamma)$, $A(\tau)$ and $f(R)$, see **Eq. (S1.4)**.

$$\Gamma \cdot G(\Gamma) = \tau \cdot A(\tau) = \frac{R^7 \cdot f(R)}{\langle R^6 \rangle} \quad (\text{S1.4})$$

The minimum information needed to characterize a distribution is to have some knowledge about its mean and variance or polydispersity index (PDI), the ratio of its variance by its square mean. Defining $\langle \Gamma \rangle$, v_G , $\langle \tau \rangle$ and v_A as the average relaxation rate, the variance of $G(\Gamma)$, the average relaxation time and the variance of $A(\tau)$, respectively; these quantities can be derived from the measured correlogram using different methods.

The simplest one is the cumulant analysis [10,11] and concerns $G(\Gamma)$. Its essence lies in a Taylor expansion of $\exp(-\Gamma \cdot \Delta t)$ around $\langle \Gamma \rangle$ for $\Delta t \rightarrow 0$, with $\langle \Gamma \rangle = \int_0^\infty \Gamma \cdot G(\Gamma) \cdot d\Gamma$ (see **Eq. S1.5**).

$$\begin{aligned} \exp(-\Gamma \cdot \Delta t) &= \exp(-\langle \Gamma \rangle \cdot \Delta t) \cdot \exp[-(\Gamma - \langle \Gamma \rangle) \cdot \Delta t] \\ &= \exp(-\langle \Gamma \rangle \cdot \Delta t) \\ &\cdot \left(1 - (\Gamma - \langle \Gamma \rangle) \cdot \Delta t + \frac{(\Gamma - \langle \Gamma \rangle)^2}{2!} \cdot \Delta t^2 - \frac{(\Gamma - \langle \Gamma \rangle)^3}{3!} \cdot \Delta t^3 + \dots \right), \Delta t \rightarrow 0 \end{aligned} \quad (\text{S1.5})$$

Substituting the expression of $\exp(-\Gamma \cdot \Delta t)$ given by **Eq. (S1.5)** into **Eq. (S1.2)** leads to a simple polynomial expression for $\ln(g_1(q \rightarrow 0, \Delta t \rightarrow 0))$, see **Eq. (S1.6)**.

$$\ln(g_1(q, \Delta t \rightarrow 0)) = -\langle \Gamma \rangle \cdot \Delta t + \frac{v_G}{2} \cdot \Delta t^2 + \dots \quad (\text{S1.6})$$

with $v_G = \int_0^\infty (\Gamma - \langle \Gamma \rangle)^2 \cdot G(\Gamma) \cdot d\Gamma$, the variance of $G(\Gamma)$.

Another approach consists in extracting the function $A(\tau)$ or $G(\Gamma)$ by performing an inverse Laplace transform (ILT) of $g_1(q, \Delta t)$ or $g_2(q, \Delta t) - 1$. An ILT is a very delicate and ill-conditioned

mathematical routine, it is highly sensitive to the noise in the data [12]. Many algorithms exist like REPES [13], CONTIN [14], SBL [15] or the recently developed CORENN [16]. All these methods use a regularizing term to smooth the solution and to limit the appearance of spurious peaks in the distribution due to the noise. CONTIN is generally used to extract $A(\tau)$ and it is often implemented in DLS software. Then, from $A(\tau)$, $\langle\tau\rangle$ and v_A are calculated. But $G(\Gamma)$ and its first two moments can also be obtained that way. ILT routines does not provide a continuous mathematical expression for distribution functions. They have the form of a histogram sampled on a logarithmic grid of relaxation times or rates. Then using **Eq. (S1.4)** to derive $f(R)$ is very risky as it involves the seventh power of R ! This can only be made if an adequate continuous mathematical expression is used that best fit relaxation rate or time distributions.

From $\langle\Gamma\rangle$, in the low q limit, a z-average diffusion coefficient, $\langle D \rangle_z$, is obtained (**Eq. (S1.7)**). It is called a z-average due to the square volume of the particle ($\propto R^6$) that weighs each diffusion coefficient.

$$\frac{\langle\Gamma\rangle}{q^2} = \frac{\int_0^\infty D \cdot R^6 \cdot f(R) \cdot dR}{\langle R^6 \rangle} = \langle D \rangle_z \quad (\text{S1.7})$$

As D is inversely proportional to R , the average hydrodynamic radius corresponding to $\langle D \rangle_z$ is not the z-average hydrodynamic radius but the inverse of the z-average inverse hydrodynamic radius (**Eq. (S1.8)**). This quantity is abusively called a z-average hydrodynamic radius but should formally be written as $\langle 1/R \rangle_z^{-1}$. It is weighted by R^5 and not R^6 . The polydispersity index of $G(\Gamma)$, PDI_G , is given by **Eq. S1.9**.

$$\langle 1/R \rangle_z^{-1} = \frac{k_B \cdot T \cdot q^2}{6\pi \cdot \eta \cdot \langle\Gamma\rangle} = \frac{\langle R^6 \rangle}{\langle R^5 \rangle} \quad (\text{S1.8})$$

$$\text{PDI}_G = \frac{v_G}{\langle\Gamma\rangle^2} = \frac{\langle R^4 \rangle \cdot \langle R^6 \rangle}{\langle R^5 \rangle^2} - 1 \quad (\text{S1.9})$$

From $\langle\tau\rangle$, the “real” z-average hydrodynamic radius $\langle R \rangle_z$ is obtained (**Eq. (S1.10)**) and the polydispersity index of $A(\tau)$ is given by Eq. (10).

$$\langle R \rangle_z = \frac{k_B \cdot T \cdot q^2 \cdot \langle\tau\rangle}{6\pi \cdot \eta} = \frac{\langle R^7 \rangle}{\langle R^6 \rangle} \quad (\text{S1.10})$$

$$\text{PDI}_A = \frac{\langle R^6 \rangle \cdot \langle R^8 \rangle}{\langle R^7 \rangle^2} - 1 \quad (\text{S1.11})$$

Due to the moments involved in **Eq. (S1.8)** and **Eq. (S1.10)**, one can easily see that $\langle 1/R \rangle_z^{-1}$ is always smaller than $\langle R \rangle_z$ for a polydisperse dispersion.

From both methods (cumulant or ILT), average values are obtained with rather good accuracy while the determination of variances (thus PDIs) are less reliable.

Finally, it is worth to note that a 3rd polydispersity index can easily be obtained from the knowledge of both average radii. It will be named PDI*. Its expression is given by **Eq. (S1.12)**. It is more robust than PDI_G or PDI_A as it results from the ratio of two rather accurate values.

$$\text{PDI}^* = \frac{\langle R \rangle_z}{\langle 1/R \rangle_z^{-1}} - 1 = \frac{\langle R^5 \rangle \cdot \langle R^7 \rangle}{\langle R^6 \rangle^2} - 1 \quad (\text{S1.12})$$

These 3 PDIs involve various moments of $f(R)$ and relations between them strongly depend on the exact shape of the number size distribution. They are all equal if $f(R)$ is a lognormal distribution.

For multimodal distributions (having two or more individualized peaks), ILT routines enable the same kind of calculation for each mode, while the cumulant analysis will only give some information about the global distribution. From the knowledge of individual $A(\tau)$, it is easy to compute corresponding $G(\Gamma)$ and to access $\langle 1/R \rangle_z^{-1}$ and PDI_G for each peak. But this procedure is questionable as it is very dependent on the regularization parameter used to perform the ILT. Some prior knowledge on the NP dispersion is highly recommended to be confident with ILT results.

S2. Monte-Carlo simulation of a FRAP experiment

Considering a cylindrical symmetry and an isotropic diffusion, the temporal evolution of the fluorescence recovery is described by the experimental intensity radial profile from the center of the ROI, $I(r, t)$, where r represents the distance to the center of the ROI and t the time after the initial bleach. In the following, $I(r, t)$ is normalized by I_0 and takes values between 0 and 1. The average fluorescence intensity in the ROI at time t is $I_{\text{ROI}}(t)$. To partly suppress the intrinsic noise in confocal images, $n=6$ independent experiments are performed at various locations in the sample and are then average.

The Monte-Carlo (MC) simulation mimics the recovery of the experimental system by modelling the uncorrelated random displacements of the fluorescent particles in each pixel of the image. At MC time $t_{\text{MC}} = 0$, the simulated image is initialized with a particle number per pixel distributed on a Poisson law with parameter $N \cdot I(r, 0)$, where N is an integer representing the average number of particles per pixel at equilibrium before the bleach. The use of a Poisson distribution gives a more realistic description of the noise present in real confocal images, as it is essentially a photon counting problem. Thus, the 1st post-bleach simulated image is very close to the experimental one, except for some statistical fluctuations (see **Figs S2.1** (a) and (b) for comparison). Then, at each MC step, every particle in every pixel moves simultaneously into an adjacent pixel chosen randomly among the four possible, with the probability $1/4$. This uncorrelated random displacement of particles is also the assumption made to derive Fick's laws. After each MC step, pixels located at the image border are reinitialized with a particle number distributed on a Poisson law with parameter N , while inner pixels retain the particle amount resulting from previous random displacements. Then t_{MC} is incremented by 1 and another MC step is performed and so on... **Fig. S2.2** shows a schematic representation of the MC algorithm at a given MC step.

Maintaining the boundary of the simulated image at a constant chemical potential ensures the return to the thermal equilibrium and drives the recovery by supplying the system with “fresh” particles. The MC simulation leads to a series of simulated images from which normalized radial profiles and average ROI intensities can be extracted. The linear size l of a pixel is known and depends on the optical setup of the microscope. Then, the average physical time t_0 needed for a particle to leave a pixel and enter one of its four neighbors is $t_0 = l^2/(4 \cdot D)$, where D is the diffusion coefficient of a particle. Thus, t_0 corresponds to the physical duration of a MC step. It leads to the relation between t_{MC} and t (**Eq. (S2.1)**).

$$t_{\text{MC}} = \frac{t}{t_0} = \frac{4 \cdot D}{l^2} \cdot t \quad (\text{S2.1})$$

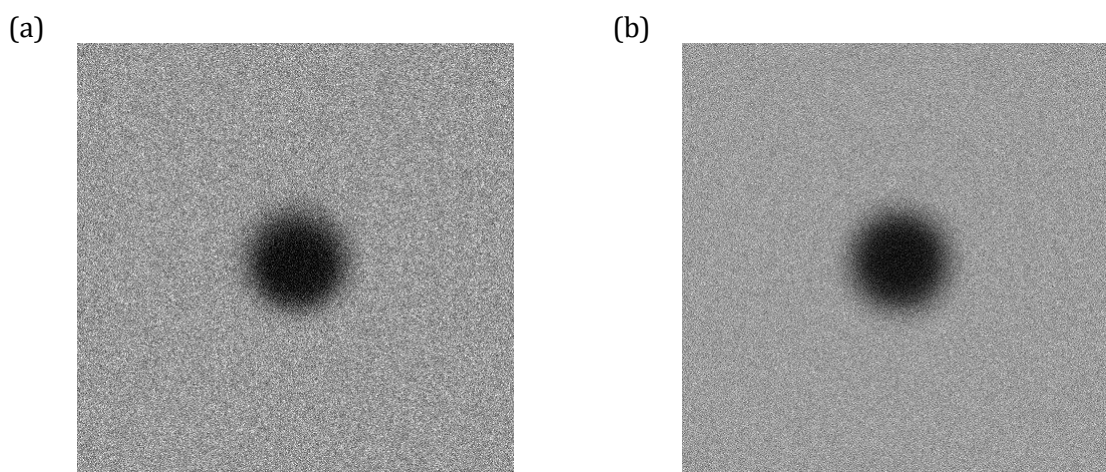


Figure S2.1. (a) The averaged signal from $n=6$ confocal images recorded just after the bleach of DiI-loaded Kolliphor® HS15 micelles in water at 30°C. The image is 435×435 pixels, with pixel size $l = 0.65 \mu\text{m}$. The ROI is $60 \mu\text{m}$ diameter. (b) Reconstructed image from the experimental radial profile using a Poisson distribution with $N = 100$.

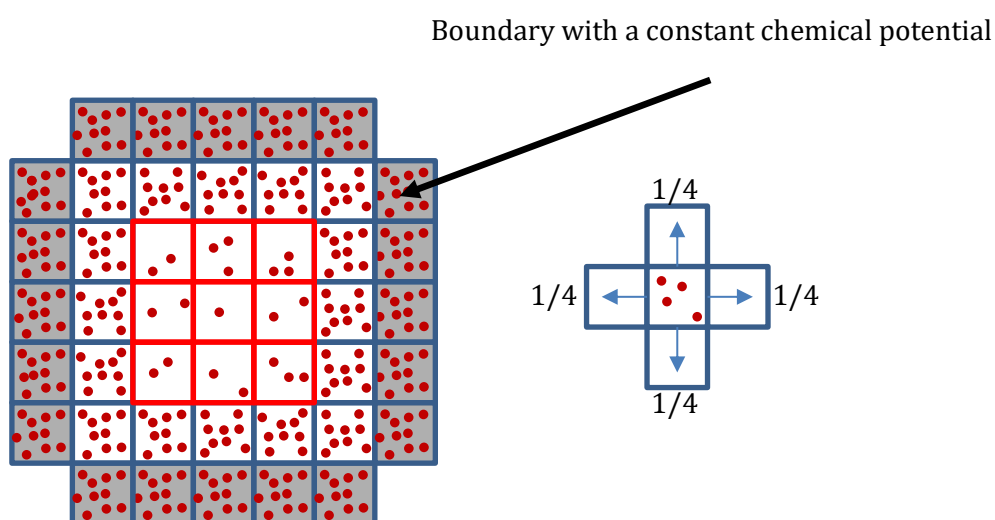


Figure S2.2. Schematic representation of the Monte Carlo algorithm.

Thus, identifying MC images that best fit each experimental image, using either radial profiles or average ROI intensities, enable the determination of D by plotting the corresponding t_{MC} as a function of t (**Eq. (S2.1)**). A value of N between 100 and 200 particles is sufficient to model the fluorescence recovery with a good accuracy. **Fig. S2.3** shows an example for a Kolliphor® HS15 solution using radial profiles. The inset in **Fig. S1.3** shows the resulting linear relation between t_{MC} and t . In this experiment, $l = 0.65 \mu\text{m}$. A linear fit to the data gives $D = 55.5 \pm 0.5 \mu\text{m}^2/\text{s}$, corresponding to a hydrodynamic radius close to 5 nm, which is in good agreement with DLS and

DOSY measurements (see the main paper). Due to the high noise level in the experimental data, the use of the radial profiles is increasingly imprecise at larger times as they vary less with time. But the MC approach is still operant if the evolution of the average ROI intensity is instead considered.

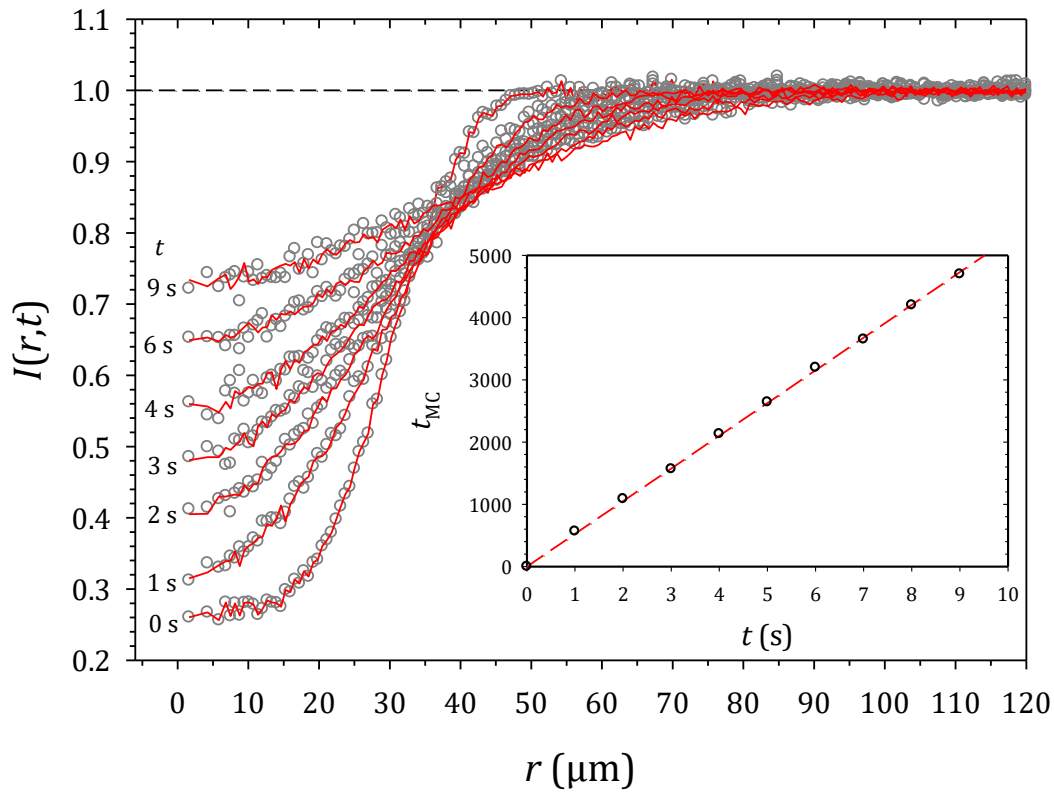


Figure S2.3. FRAP experiment on DiI-loaded Kolliphor® HS15 micelles in water at 30°C. Circles represent experimental radial profiles (averaged over $n=6$) for various times t after the bleach, as indicated in the figure. Red lines represent MC radial profiles that best fit the experimental data. The corresponding t_{MC} are plotted as a function of t in the inset. The red dashed line represents a linear fit to the data.

Fig. S2.4 shows the evolution of the experimental average recovery ratio in the ROI, $\langle r_{ROI}(t) \rangle$ as a function of time t . Using the diffusion coefficient calculated previously, we see that the MC evolution perfectly fits the experimental one all along the recovery process.

This demonstrate the relevance of such an approach to process FRAP data whatever the initial bleached profile is. Moreover, contrary to the Kang approach [17] that fit the complete recovery curve of the ROI, it is not necessary to perform long experiments to reach the final plateau. An accurate estimate of D can be calculated using only the first dozen images. Therefore, to have a better statistic, a larger ROI can be used. This is not possible with the Kang approach, as the time needed to recover a given amount of fluorescence is proportional to the square of the ROI size.

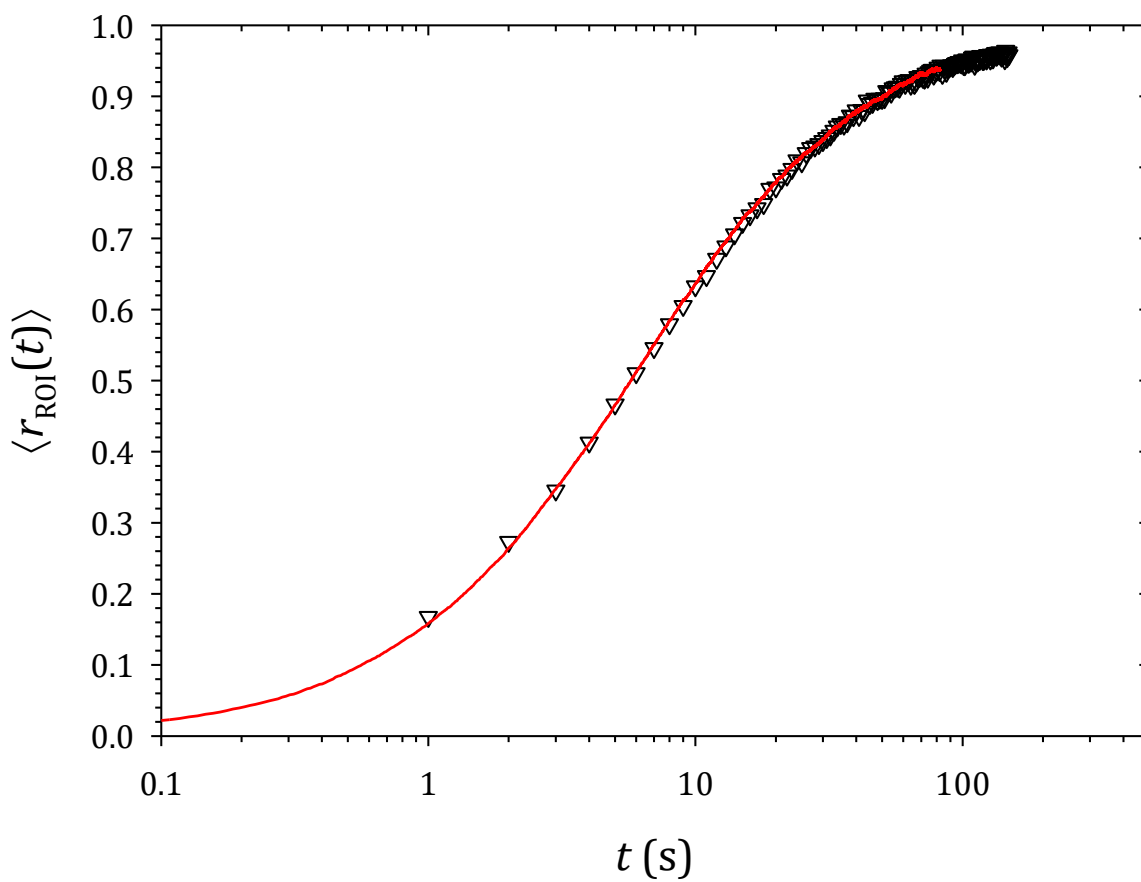


Fig. S2.4. FRAP experiment on Kolliphor® HS15 micelles loaded with DiI, in water at 30°C. Triangles represent average experimental results (n=6). The red line represents MC simulation results using the correspondence between t_{MC} and t previously calculated.

S3. NMR ¹H Kolliphor® HS15 spectrum elucidation

2D NMR spectra of Kolliphor® HS15 were recorded by using a 500MHz Avance III HD NMR spectrometer (Bruker, France) equipped with a 5mm Broadband Observe probe. Kolliphor® HS15 was dissolved in CDCl₃ (1% w/v). ¹H, correlation spectroscopy (COSY), heteronuclear single quantum coherence spectroscopy (HSQC) and heteronuclear multiple bond correlation (HMBC) spectra were recorded at 25 °C.

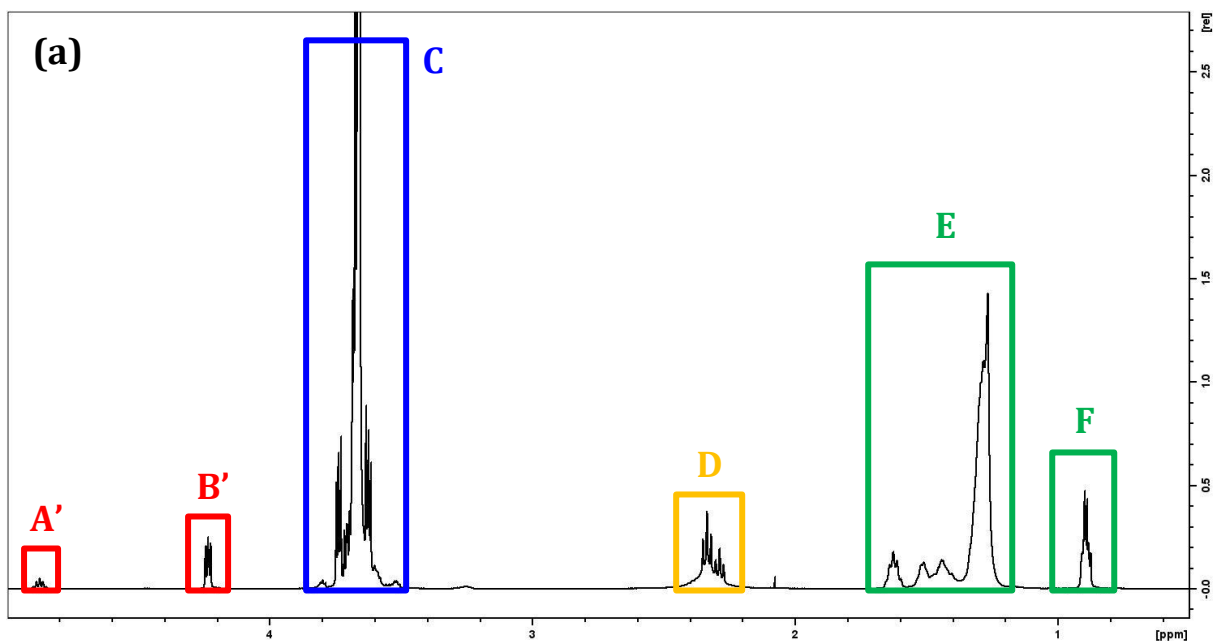
The HMBC spectrum was acquired with the *hmbcgpplndqf* Bruker sequence. The spectral windows for ¹H and ¹³C axes were 2994 and 25102 Hz, respectively. Data were collected using a 1024 × 512 matrix, 128 scans, 1.5 s relaxation delay (d1).

The edited HSQC spectrum was acquired with the *hsqcedetgp* Bruker sequence. The spectral windows for ¹H and ¹³C axes were 2994 and 20709 Hz, respectively. Data were collected using a 512 × 512 matrix, 16 scans, and 1.5 s relaxation delay (d1).

The COSY spectrum was acquired with the *cosygpppqf* Bruker sequence. The spectral window was 748 Hz in both directions, centered on the 3.7 ppm area. Data were collected using a 2048 × 512 matrix, 16 scans, 1.7 s relaxation delay (d1).

The ¹H NMR spectrum of Kolliphor® HS15 (**Fig. S3.1(a)**) was elucidated based on literature [18] and using two dimensional (COSY, HSQC, and HMBC) 2D NMR spectra. A HMBC NMR experiment is a 2D experiment that shows ¹H/¹³C multiple-bond connectivity (**Fig. S3.2**). A HSQC NMR experiment is a 2D experiment that shows ¹H /¹³C single bond connectivity (**Fig. S3.3**). A COSY NMR experiment is a 2D experiment that shows J-coupled protons (see **Fig. S3.4**).

Around 0.9ppm ¹H signals: The chemical shifts and the correlation in the HMBC spectrum observed between (δ H 0.8-1.0)/ (δ C 13-38) confirmed that these protons are characteristics of alkane chains (**Fig. S3.2**). Furthermore, as the multiplicity edited HSQC (**Fig. S3.3**) differentiates upon phase information CH and CH₃ (in green) apart CH₂ groups (in blue) correlations, the 0.9ppm signals can be identified to a CH or CH₃, confirming that the 0.9ppm signals correspond to F protons of the Kolliphor® HS15 (**Fig. S3.1(b)**).



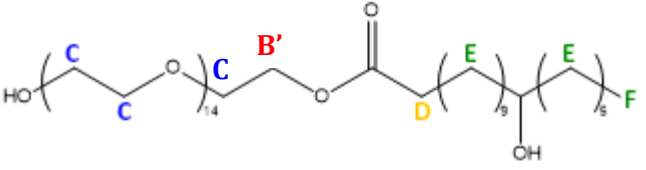
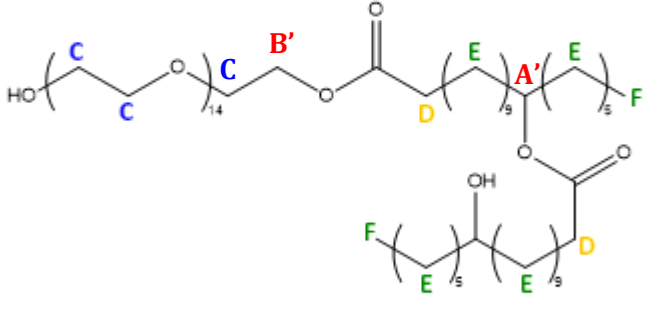
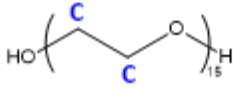
| (b) | Name | Chemicals with NMR peak codes |
|-----------------------|----------------------|--|
| Kolliphor® HS15 (Kol) | Mono-ester (PEG-HS1) |  |
| | Di-ester (PEG-HS2) |  |
| | PEG |  |

Figure S3.1. (a) Kolliphor® HS15 ^1H NMR spectrum in CDCl_3 . (b) Corresponding protons in the molecules.

Around 1.45 ppm ^1H signals: The chemical shifts and the main correlation in the HMBC spectrum observed between (δH 1.11-1.8) / (δC 13-38) confirmed that these protons are characteristics of alkane chains (**Fig. S3.2**). The blue correlations in the edited HSQC observed for these

resonances, corresponding to CH₂ from the PEG (**Fig. S3.3**), confirm that these peaks correspond to E protons of the Kolliphor® HS15 (**Fig. S3.1(b)**).

Around 2.35 ppm ¹H signals: In the HMBC spectrum, a correlation was observed between (δ H 2.35)/ (δ C 174) which confirmed that these protons are close to the carbonyl function (**Fig. S3.2**). The blue correlations in the edited HSQC are observed for 2.35 ppm resonances (**Fig. S3.3**), corresponding to CH₂, confirm that these peaks correspond to D protons of the Kolliphor® HS15 (**Fig. S3.1(b)**).

Around 3.7 ppm ¹H signals: In the HMBC spectrum, a correlation was observed between (δ H 3.7)/ (δ C 71) which confirmed that these protons are close to the alcohols or ethers functions (**Fig. S3.2**). These signals correspond to PEG protons. The blue correlations in the edited HSQC (**Fig. S3.3**) are observed for these resonances, corresponding to CH₂ from the PEG, confirm that these peaks correspond to C protons of the Kolliphor® HS15 (**Fig. S3.1(b)**).

Around 4.2 ppm ¹H signals: In the HMBC spectrum, a correlation was observed between (δ H 4.2)/ (δ C 69 and 174) which confirmed that these protons are close to carbons involved in PEG chains and the ester function (**Fig. S3.2**). The blue correlation in the edited HSQC (**Fig. S3.3**) corresponds to CH₂. Finally, the correlation is observed on the COSY (**Fig. S3.4**) between this signal and the PEG signal around 3.7 ppm confirms that the 4.2 ppm signals correspond to B' protons of the Kolliphor® HS15 (**Fig. S3.1(b)**).

Around 4.88 ppm ¹H signals: In the HMBC spectrum, correlations were observed between (δ H 4.88)/ (δ C 25, 34 174), which confirmed that these protons are close to the aliphatic carbons (carrying E protons) and the ester function (**Fig. S3.2**). The green correlation in the edited HSQC (**Fig. S3.3**) corresponds to CH, confirming that the 4.88 ppm signals correspond to A' protons of the Kolliphor® HS15 (**Fig. S3.1(b)**).

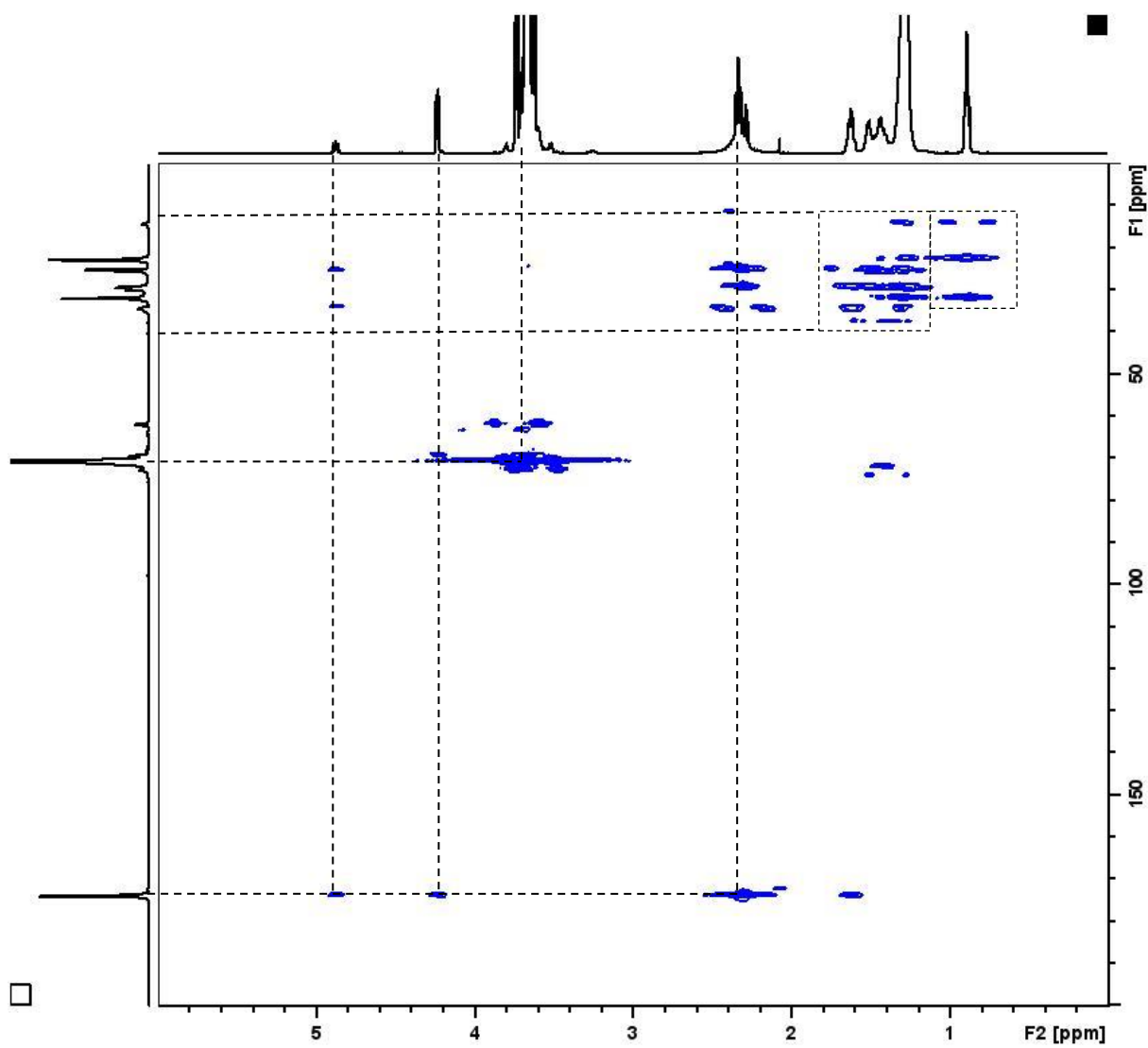


Figure S3.2. 2D HMBC spectrum of Kolliphor® HS15 in CDCl₃.

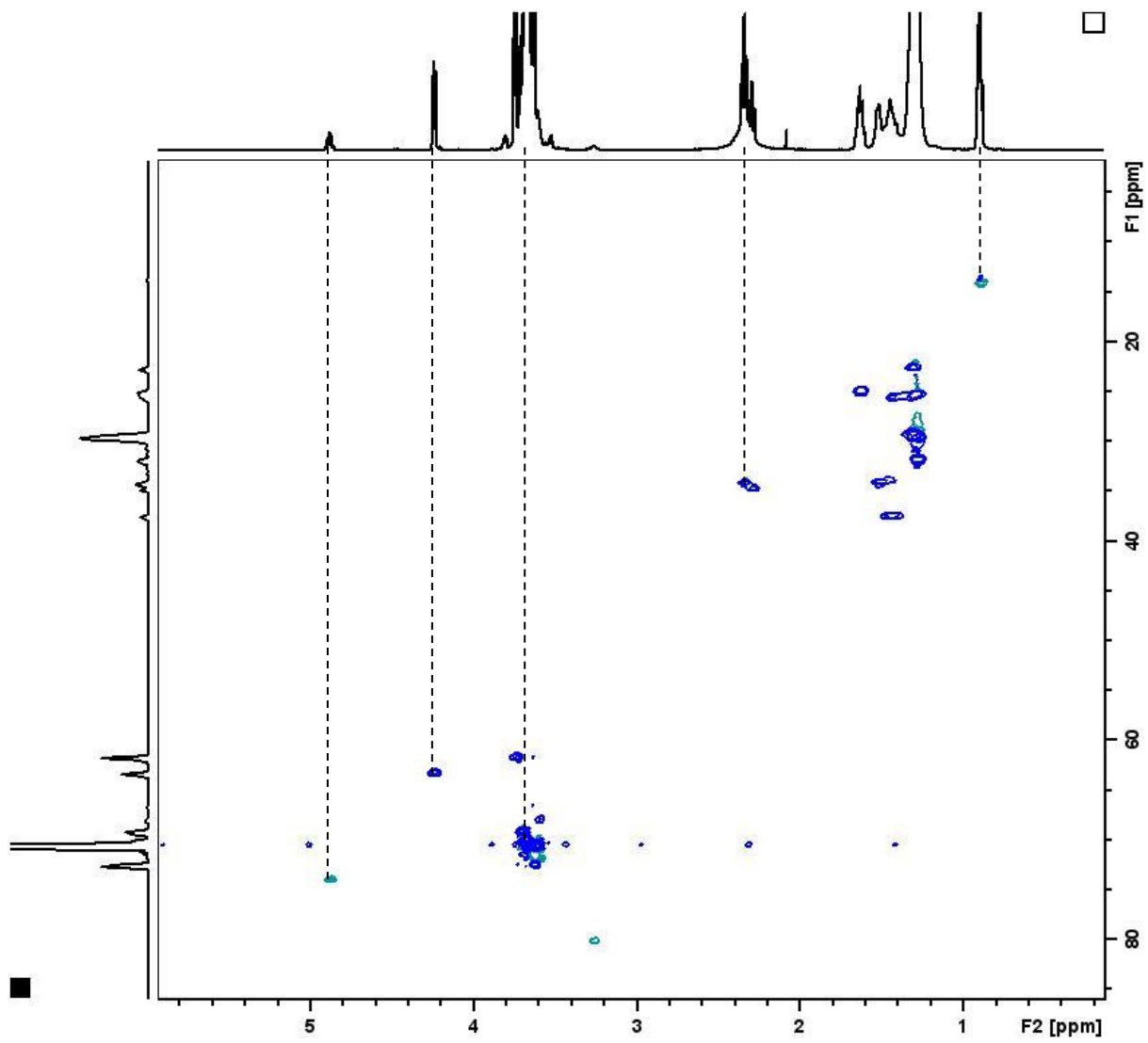


Figure S3.3. 2D HSQC spectrum of Kolliphor® HS15 in CDCl_3 .

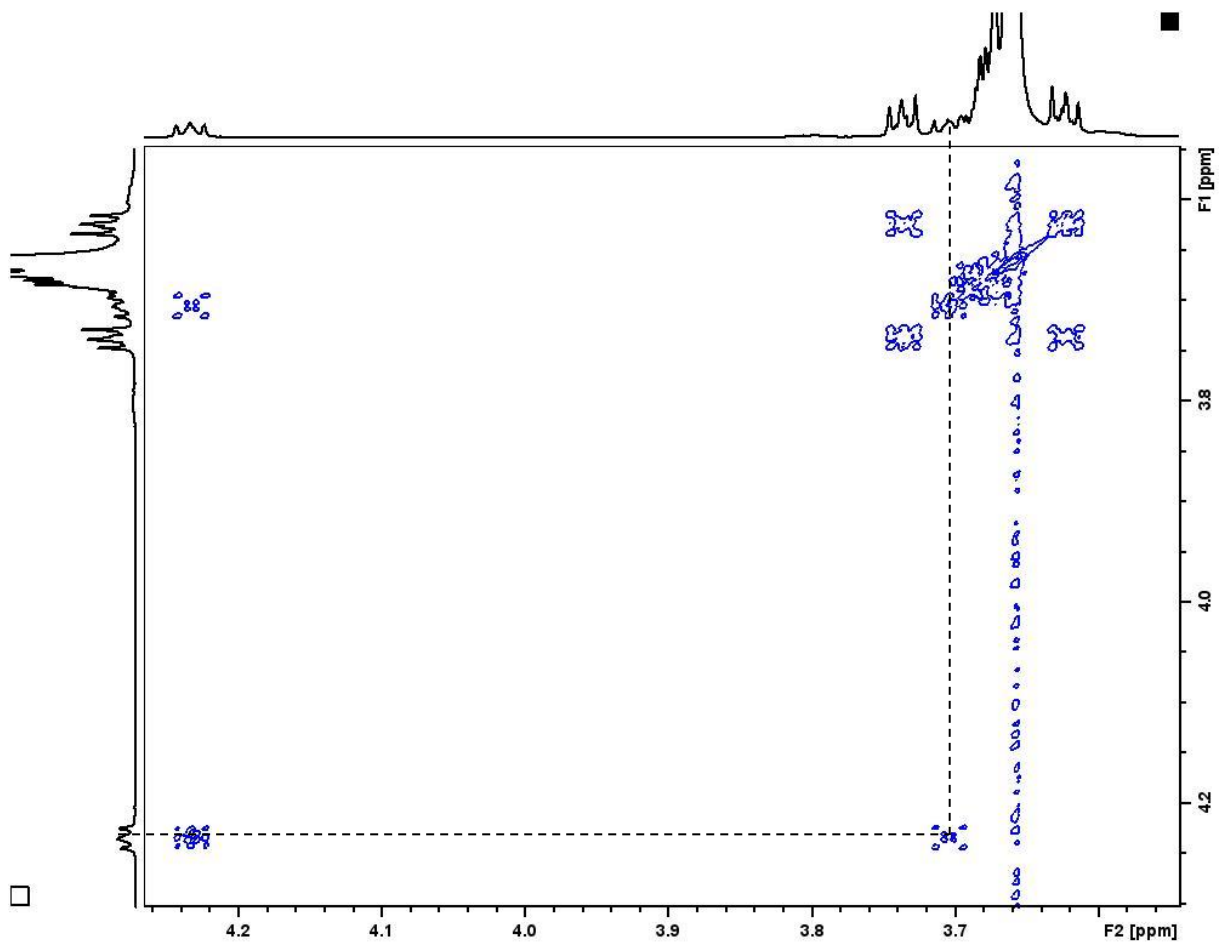


Figure S3.4. 2D COSY spectrum of Kolliphor® HS15 in CDCl_3 .

S4. NMR: component contributions in SCORE analysis

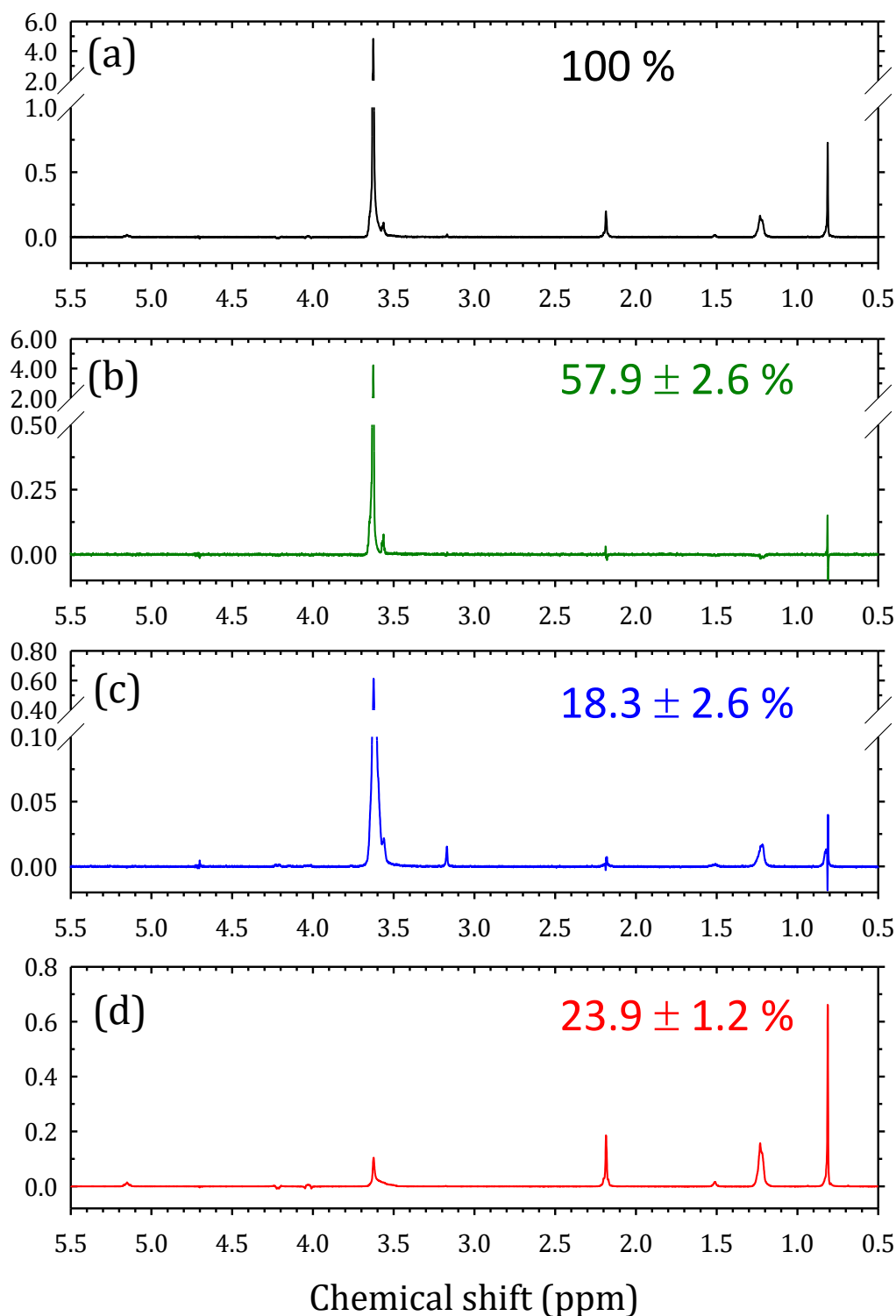


Figure S4.1. NMR diffusometry of a D₂O-LNC suspension. Contributions of each diffusing component (b) fast, (c) medium and (d) slow to the total ¹H spectrum (a) for the 1% v/v sample D₂O-LNC. Same color codes as in **Fig. 5** of the paper. Numerical values indicate the average weight of each diffusing component to the total spectrum for the four different concentrations. The peak at 4.70 ppm, corresponding to water traces (see **Fig 4** in the paper), was excluded from the SCORE analysis. Y-Scales are different in (c) and (b) to magnify small peaks.

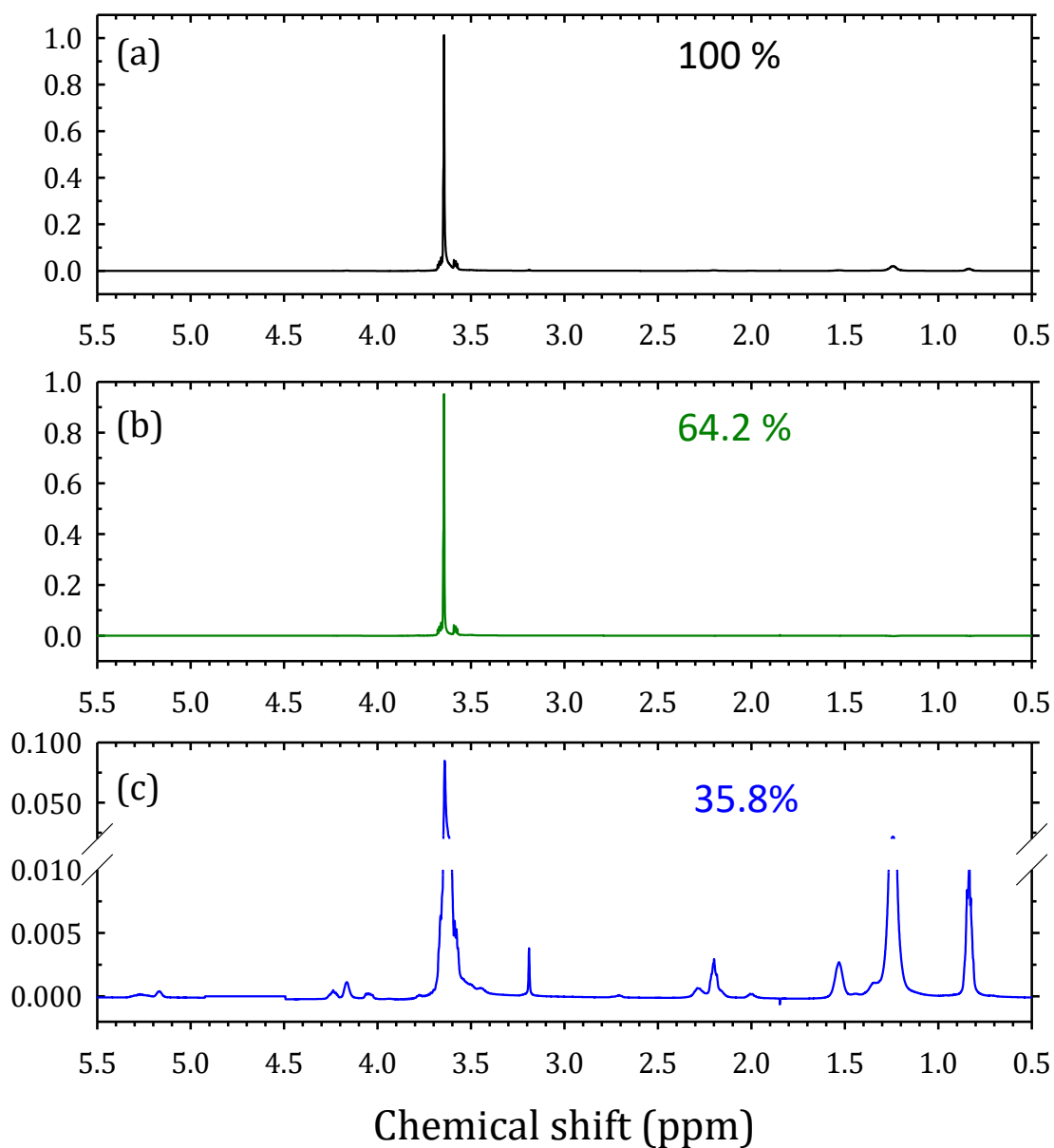


Figure S4.2. NMR diffusometry of the undernatant of a D₂O-LNC suspension. Contributions of each component (b) fast, (c) medium to the total ^1H spectrum (a) for the undernatant of an ultracentrifuged D₂O-LNC suspension. Values indicate the weight of each component to the total spectrum. The water peak at 4.70 ppm has been excluded for the SCORE analysis. Y-Scales are different in (c) to magnify small resonant peaks.

S5. qNMR: Calibration curve for Cap dosage in undernatants

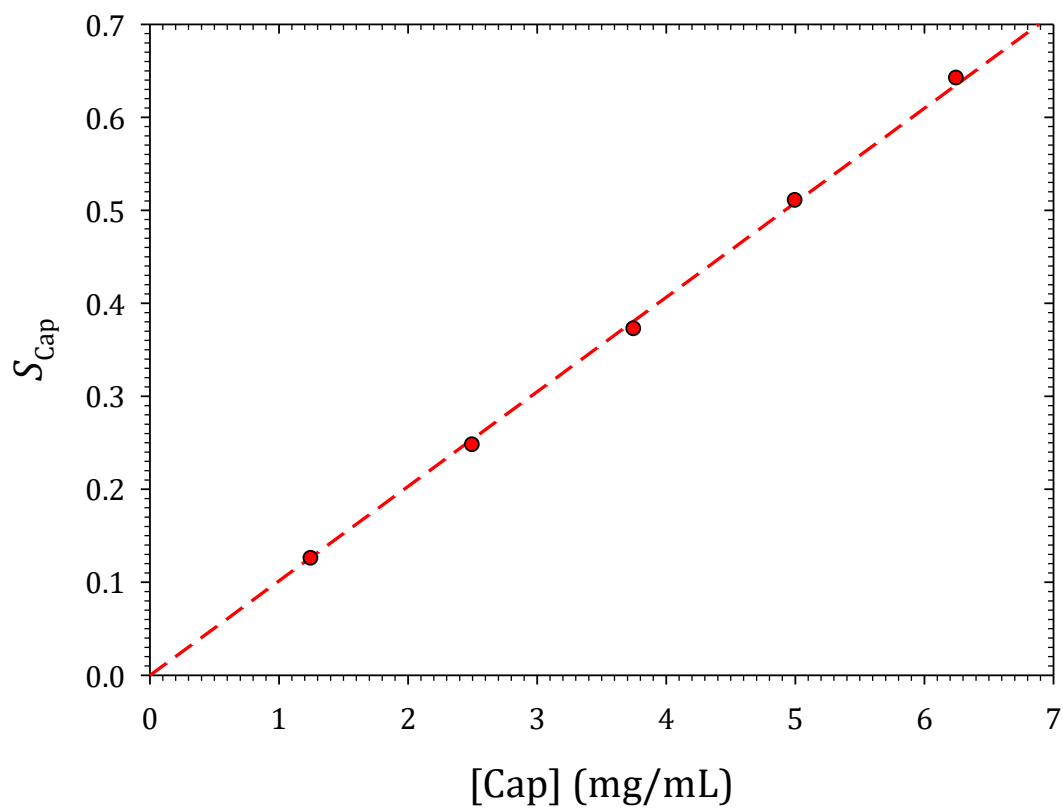


Figure S5.1. NMR: Calibration curve for Captex 8000 (Cap) obtained from ^1H NMR spectra for various concentrations in THFd. Peak clusters A and B were used to compute S_{Cap} (see **Fig. 7** and **Table 4** in the paper). A linear fit (red dashed line) to the data (red circles) gives a slope of 0.102 ± 0.003 mL/mg with a coefficient of determination, $r^2 = 0.9989$.

S6. DLS: Correspondence between the scattering intensity fraction and the mass fraction for a dilute binary mixture of NPs with different sizes, same density, and same refractive index.

Here, a dilute binary mixture of spherical NPs with different sizes (R_1, R_2) and mass (m_1, m_2) is considered. The particle size ratio is defined as $\alpha = R_2/R_1 \geq 1$. The total excess intensity, I_{tot} , scattered by that mixture is simply the sum of the two contributions: $I_{\text{tot}} = N_1 \cdot I_1 + N_2 \cdot I_2$, where N_1, N_2 are the numbers of NPs of type 1 or 2 in the scattering volume respectively, and I_1, I_2 are the excess scattering intensities by single NPs of type 1 or 2, respectively. As $R_2 = \alpha \cdot R_1$, assuming both types of NPs have the same density, this leads to $m_2 = \alpha^3 \cdot m_1$. Then, assuming they also have the same refractive index, in the limit of $q \cdot R_2 \ll 1$, $I_2 = \alpha^6 \cdot I_1$. If the scattering vector is not small enough, the big NP contribution is reduced by their form factor. At very large q , and if α is large enough, using SAXS or SANS, it can even be canceled, thus revealing the presence of the small objects [19].

Defining β as the fraction of the total intensity scattered by the small NPs, it can easily be shown that the mass fraction f_m of the small NPs in the mixture is given by **Eq. (S6.1)**.

$$f_m = \frac{\beta \cdot \alpha^3}{\beta \cdot \alpha^3 + 1 - \beta} \approx 1 - \frac{1 - \beta}{\beta \cdot \alpha^3} \text{ for } \beta \cdot \alpha^3 \gg 1 \quad (\text{S6.1})$$

As an example, using a size ratio $\alpha = 10$ with a scattering intensity fraction $\beta = 0.05$ corresponds to a mass fraction $f_m = 0.981$ of small NPs in the sample! Thus, big NPs representing only 2 wt% of the matter are responsible for 95 % of the scattered intensity. This amount even falls to 0.002 wt% for $\alpha = 100$. A very small wt% of big particles can dominate the scattering signal at small angles.

Expressing β as a function of α and f_m is also very useful as it can help to predict if a population of small NPs mixed with big ones can be detected using DLS (**Eq. (S6.2)**).

$$\beta = \frac{f_m}{\alpha^3 \cdot (1 - f_m) + f_m} \quad (\text{S6.2})$$

The first example concerns Kolliphor® HS15 solution. They are supposed to contain around 30 wt% of free PEG chains with a size ratio close to $\alpha = 6$ between PEG chains and micelles. Then the contribution of free PEG chains to the total scattered intensity is around $\beta = 0.002$ and can therefore not be detected by DLS on Kol samples at a concentration above their critical micellar concentration (CMC). The second example concerns residual micelles in LNC formulations. Not considering free PEG chains, their mass fraction is estimated around $f_m = 0.18$ and the size ratio

is close to $\alpha = 4$ compared to the LNCs. The micellar contribution to the scattered intensity is therefore $\beta = 0.003$! Residual micellar structures can neither be detected using DLS on LNC samples not too much diluted so that residual surfactant molecules stay in the form of micelles (above their CMC).

Bibliography

- [1] B.J. Berne, R. Pecora, *Dynamic Light Scattering: With Applications to Chemistry, Biology, and Physics*, Dover Publications Inc., Mineola, 2003.
- [2] K.S. Schmitz, *Introduction to Dynamic Light Scattering by Macromolecules*, Academic Press, Boston, 1990. doi:10.1016/C2009-0-29091-X.
- [3] J.K.G. Dhont, *Introduction to Dynamics of Colloids*, 2nd ed., Elsevier, Amsterdam, 1996.
- [4] M. Tokuyama, I. Oppenheim, Dynamics of hard-sphere suspensions, *Phys. Rev. E* 50 (1994) R16–R19. doi:10.1103/PhysRevE.50.R16.
- [5] W.R. Bowen, A. Mongruel, Calculation of the collective diffusion coefficient of electrostatically stabilised colloidal particles, *Colloids Surfaces A Physicochem. Eng. Asp.* 138 (1998) 161–172. doi:10.1016/S0927-7757(96)03954-4.
- [6] K. Fischer, M. Schmidt, Pitfalls and novel applications of particle sizing by dynamic light scattering, *Biomaterials* 98 (2016) 79–91. doi:10.1016/j.biomaterials.2016.05.003.
- [7] M. Rubinstein, R.H. Colby, *Polymer Physics*, Oxford University Press, Oxford, 2003.
- [8] D. Lehner, H. Lindner, O. Glatter, Determination of the translational and rotational diffusion coefficients of rodlike particles using depolarized dynamic light scattering, *Langmuir* 16 (2000) 1689–1695. doi:10.1021/la9910273.
- [9] O. Glatter, *Scattering Methods and their Application in Colloid and Interface Science*, Elsevier, Amsterdam, 2018. doi:10.1016/C2016-0-04640-5.
- [10] D.E. Koppel, Analysis of macromolecular polydispersity in intensity correlation spectroscopy: The method of cumulants, *J. Chem. Phys.* 57 (1972) 4814–4820. doi:10.1063/1.1678153.
- [11] B.J. Frisken, Revisiting the method of cumulants for the analysis of dynamic light-scattering data, *Appl. Opt.* 40 (2001) 4087. doi:10.1364/AO.40.004087.

- [12] P. Rainer, Noise on photon correlation functions and its effect on data reduction algorithms, in: W. Brown (Ed.), *Dyn. Light Scatt. Method Some Appl.*, Clarendon Press, Oxford, 1993: pp. 149–176.
- [13] J. Jakeš, Regularized Positive Exponential Sum (REPES) Program - A Way of Inverting Laplace Transform Data Obtained by Dynamic Light Scattering, *Collect. Czechoslov. Chem. Commun.* 60 (1995) 1781–1797. doi:10.1135/cccc19951781.
- [14] S.W. Provencher, A constrained regularization method for inverting data represented by linear algebraic or integral equations, *Comput. Phys. Commun.* 27 (1982) 213–227. doi:10.1016/0010-4655(82)90173-4.
- [15] S.-L. Nyeo, R.R. Ansari, Sparse Bayesian learning for the Laplace transform inversion in dynamic light scattering, *J. Comput. Appl. Math.* 235 (2011) 2861–2872. doi:10.1016/j.cam.2010.12.008.
- [16] LS Instruments, *DLS Data Analysis: The CORENN Method*, (n.d.). <https://lsinstruments.ch/en/theory/dynamic-light-scattering-dls/dls-data-analysis-the-corenn-method> (accessed June 19, 2023).
- [17] M. Kang, C.A. Day, K. Drake, A.K. Kenworthy, E. DiBenedetto, A Generalization of Theory for Two-Dimensional Fluorescence Recovery after Photobleaching Applicable to Confocal Laser Scanning Microscopes, *Biophys. J.* 97 (2009) 1501–1511. doi:10.1016/j.bpj.2009.06.017.
- [18] F.D. Gunstone, J.L. Harwood, J.L. Harwood, eds., *The Lipid Handbook*, 3rd ed., CRC Press, Boca Raton, 2007. doi:10.1201/9781420009675.
- [19] L. Guyon, E. Lepeltier, J.-C. Gimel, B. Calvignac, F. Franconi, N. Lautram, A. Dupont, C. Bourgaux, P. Pigeon, P. Saulnier, G. Jaouen, C. Passirani, Importance of Combining Advanced Particle Size Analysis Techniques To Characterize Cell-Penetrating Peptide–Ferrocifen Self-Assemblies, *J. Phys. Chem. Lett.* (2019) 6613–6620. doi:10.1021/acs.jpcllett.9b01493.

Graphical Abstract

